3-22-2018

Forecasting Lightning Initiation Utilizing Dual-Polarization Radar Parameters over Washington, D.C.

Sarah A. Olsen

Forecasting Lightning Initiation Utilizing Dual-Polarization Radar Parameters over Washington, D.C.

THESIS

Sarah Allison Olsen, 2d Lt, USAF

AFIT-ENP-MS-18-M-092

DEPARTMENT OF THE AIR FORCE
AIR UNIVERSITY

AIR FORCE INSTITUTE OF TECHNOLOGY

Wright-Patterson Air Force Base, Ohio

AFIT-ENP-MS-18-M-092

FORECASTING LIGHTNING INITIATION UTILIZING DUAL-POLARIZATION RADAR PARAMETERS OVER WASHINGTON, D.C.

THESIS

Presented to the Faculty

Department of Engineering Physics

Graduate School of Engineering and Management

Air Force Institute of Technology

Air University

Air Education and Training Command

in Partial Fulfillment of the Requirements for the

Degree of Master of Science in Atmospheric Science

Sarah Allison Olsen, B.S.

2d Lt, USAF

22 March 2018

AFIT-ENP-MS-18-M-092

FORECASTING LIGHTNING INITIATION UTILIZING DUAL-POLARIZATION RADAR PARAMETERS OVER WASHINGTON, D.C.

THESIS

Sarah Allison Olsen, B.S.
2d Lt, USAF

Committee Membership:

Maj O. A. Nava, Ph.D.
Chair

Maj C. D. Lewis, Ph.D.
Member

W. P. Roeder, M.S.
Member

Abstract

Accurate forecasts of thunderstorms are vital to space launch, aviation, and public safety. Prior studies by Woodard (2011), Thurmond (2014), and Travis (2015) show that dual-polarization radar can be utilized to identify the presence of hydrometeors necessary for cloud charging. These studies emphasized that a combination of radar reflectivity (Z) and differential reflectivity (Z_{DR}) predictors have the potential to improve forecast skill of lightning initiation over methods that rely on Z alone (Roeder and Pinder, 1998; Yang and King, 2010). Travis (2015) discovered two parameters, when used together, produced the best results: $Z \geq 36.5$ dBZ and $Z_{DR} \geq 0.31$ at the -10°C height. Travis (2015) also highlighted that Z_{DR} is the preferred parameter to use in conjunction with Z as elevated Z_{DR} values are indicative of supercooled water droplets and wet ice particles which are important to the overall electrification process occurring within a cloud. This study applied the lightning initiation prediction method developed for Cape Canaveral Air Force Station (CCAFS) and NASA Kennedy Space Center (KSC) in Travis (2015) to a new location. The method was tested on 100 isolated, warm season thunderstorms spanning 5 years in and around the Washington D.C. area. Forecast metrics and lead times were calculated and compared to the results of Travis (2015). The results of this study concluded that the lightning initiation prediction algorithm from Travis (2015) for CCAFS/KSC does not perform well for the Washington, D.C. area. This implies that one lightning initiation prediction method cannot be applied across the entire national NEXRAD network.

Acknowledgements

I would like to extend my gratitude to my thesis advisor for his patience, guidance and wisdom throughout the research and writing process. Thank you for challenging me and pushing me to academic limits that I never thought possible. I would also like to thank my committee members. Your insight, knowledge, and perspective always served as a check to ensure I fully understood the reason behind my methods. Additionally, this thesis would not have been possible without your guidance and assistance from the 45th Weather Squadron.

I would also like to thank my classmates. It would not have been possible to complete AFIT without all of your support. Thank you all for setting the example of the type of officer I want to be when I move into Air Force weather operations. In addition, I would like to extend my deepest gratitude to my lightning cessation counterpart. Overcoming the obstacles of AFIT would not have been possible without your constant support and friendship. There are no words to adequately convey how thankful I am for all that you have done for me. Good luck to all of you at your next assignments!

Finally, I would like to thank my husband. Grateful doesn't even begin to express how I feel about the love and support you always show me, even from 1,000 miles away. I can't wait to finally spend more time with you when we get stationed together at our next assignment!

Sarah Allison Olsen

Table of Contents

Page

List of Figures

List of Tables

List of Abbreviations

45WS 45th Weather Squadron

4DLSS Four Dimensional Lightning Surveillance System

CAPE Convective Available Potential Energy

CCAFS Cape Canaveral Air Force Station

CGLSS Cloud-to-Ground Lightning Surveillance System

CI Confidence Interval

CR Correct Rejection

CSI Critical Success Index

dB Decibels

DNE Does Not Exist

FA False Alarm

FAR False Alarm Ratio

GR2Analyst Gibson Ridge Level 2 Radar Analyst

HCA Hydrometeor Classification Algorithm

KAKQ Wakefield, VA

KDOX Dover Air Force Base, DE

KLWX Sterling, VA

KMLB Melbourne, FL

KSC Kennedy Space Center

LDAR Lightning Detection and Ranging

LMA Lightning Mapping Array

NASA National Aeronautics and Space Administration

NCDC National Climatic Data Center

NCEI National Centers for Environmental Information

NEXRAD Next Generation Weather Radar

NLDN National Lightning Detection Network

NOAA National Oceanic and Atmospheric Administration

NWS National Weather Service

OUI Operational Utility Index

PAFB Patrick Air Force Base

PFA Probability of False Alarms

PID Particle Identification

POD Probability of Detection

POFA Probability of False Alarms

POFD Probability of False Detection

radar Radio Detection and Ranging

SCIT Storm Cell Identification and Tracking

TSS True Skill Statistic

USAF United States Air Force

VCP Volume Coverage Pattern

VIL Vertically Integrated Liquid

WDSS-II Warning Decision Support System-Integrated Information

WSR-57 Weather Surveillance Radars-1957

WSR-74C Weather Surveillance Radars-1974 C-Band

WSR-74S Weather Surveillance Radars-1974 S-Band

WSR-88D Weather Surveillance Radars-1988 Doppler

WWII World War II

I. Introduction

This chapter will introduce the motive behind this study. It will also briefly discuss the objective of the research. Finally, the introduction chapter will provide a preview of the overall layout of the study that will serve as a guide moving forward.

1.1. Motivation

The occurrence of lightning is one of Earth's natural dangers and each day approximately 50,000 thunderstorms occur around the globe (Ahrens, 2014). As a result of these thunderstorms, approximately 100 cloud-to-ground lightning strikes hit the surface of the earth each second (about 8 million per day) (National Geographic, 2018). Over the past 30 years, the United States has averaged around 55 lightning fatalities and 300 injuries per year (Roeder, 2012; NWS, 2017a). Although there have been recent reductions in lightning-related injuries and fatalities, lightning continues to remain a deadly and costly weather phenomenon in the United States (Holle, 2016). Research conducted by the National Lightning Safety Institute (2014) suggests realistic lightning costs and losses may exceed $8-10 billion per year in the United States alone. Continuing research into this deadly and costly force of nature will allow for additional time to prepare and respond with effective safety measures.

Lightning initiation is among the biggest forecast challenges facing the Air Force's 45th Weather Squadron (45WS). The 45WS is responsible for supporting space launch operations at Cape Canaveral Air Force Station (CCAFS), Kennedy Space Center (KSC), and Patrick Air Force Base (PAFB). Determining the most accurate lightning initiation prediction methods is vital to safeguard these areas, which include over $20 billion of facilities and over 25,000 personnel (Travis, 2015). While lightning initiation prediction methods currently exist for the CCAFS/KSC/PAFB

area, these methods can be improved upon and possibly applied to different locations to increase lightning forecast accuracy across the country. Overall, accurate forecasts of thunderstorms are crucial for space launch, aviation, and public safety.

1.2. Research Objective

While prior studies have primarily focused on atmospheric conditions preceding lightning initiation, more work is needed to apply dual-polarization parameters to this challenging problem. This study will verify the lightning initiation prediction method developed by the Air Force Institute of Technology for CCAFS and KSC in Travis (2015). The best performing thresholds for the CCAFS/KSC area based on forecast metrics and lead time will be applied to the Washington, D.C. region. If this lightning initiation prediction method verifies well at this new location, that will build confidence for use of the method at CCAFS/KSC and lend credence for use at other locations and eventual implementation as a new product in the Next Generation Weather Radar (NEXRAD) network.

1.3. Preview

This chapter introduced the motivation for the study, the ultimate objective of the research and briefly covered the scope of the problem. Chapter II covers the background information of several topics applicable to lightning initiation utilized throughout the research process. It also discusses prior research already conducted on this topic. Chapter III explains the archived radar and lightning data used to build the dataset for analysis. It also details the methodology for analysis. Chapter IV provides the results of the data analysis. Finally, Chapter V discusses the conclusions drawn from the results and also gives recommendations for future work.

II. Background

This chapter will cover in-depth several topics mentioned and utilized throughout the research process applicable to lightning initiation. These topics include the basics of lightning, weather radar, lightning detection and previous research contributing to this study. The chapter can serve as a reference when processes or topics are unclear throughout the rest of the recorded research process.

2.1. Lightning

Although lightning is a common phenomenon familiar to many, the dynamics behind this force of nature are quite complex. The continuation of lightning research is crucial to safeguard people and assets worldwide. This section will introduce the basics of cloud electrification followed by the process behind lightning discharge.

2.1.1 Cloud Electrification

The electrification of a developing single-cell thunderstorm is the result of a combination of several processes. Inductive charging of rebounding particles, ion capture mechanisms, convection methods, and non-inductive charging are all hypothesized to cause cloud electrification (MacGorman and Rust, 1998). However, most occur too slowly to explain the electrification of a single-cell thunderstorm over its usually short lifespan. Saunders (2008) provides a review of a broad selection of charge separation mechanisms in clouds and concludes that inductive and non-inductive charging are the most feasible options. Inductive charging relies on the pre-existing vertical electric field to induce charges on the hydrometeors. Particle rebounds can then separate the charge and strengthen the electric field. Initially, the electric field may be due to the downward directed fair weather field resulting from the negatively charged ground sur-

face and positive charges in the atmosphere (Saunders, 2008). Non-inductive charging is the only hypothesis of the four mentioned above that reinforces the process of rapid charge buildup. In contrast, as the name implies, non-inductive charging does not require the hydrometeors involved in the charging process to be polarized by the ambient electric field. Additionally, non-inductive charging is currently the most widely accepted theory as the dominant electrification process within a thunderstorm (Wallace and Hobbs, 2006).

The mature stage of a single-cell thunderstorm is characterized by the presence of both an updraft and a downdraft. Figure 1 gives an example of a typical updraft and downdraft within a single-cell thunderstorm. According to Deierling et al. (2005; 2008), the production of lightning is directly proportional to mass upward flux of ice crystals and the downward mass flux of graupel. Each of these fluxes are tied to the updrafts and downdrafts of the single-cell thunderstorm. Charge is generated within the cloud when collisions occur between falling graupel and stationary to upward moving ice crystals that make up various portions of the cloud (MacGorman and Rust, 1998).

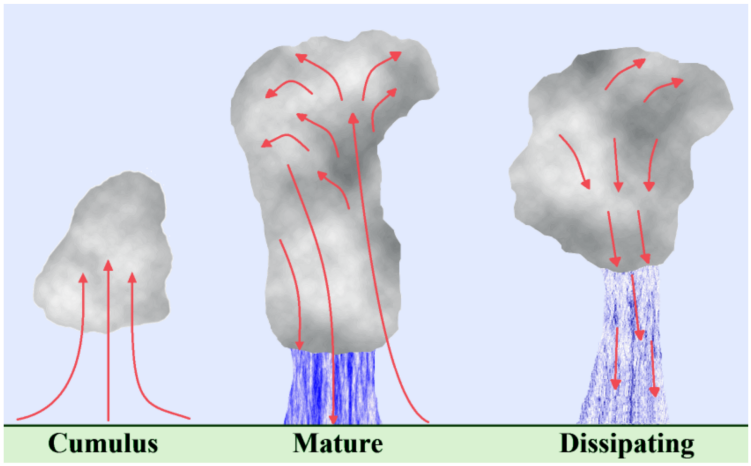

Figure 1. A depiction of the three stages of single-cell thunderstorm development. The mature stage clearly shows the upward and downward flow of the updraft and downdraft. Image from Travis (2015).

In the collision process, graupel (gaining mass through accretion) descends as it becomes too heavy for the updraft to hold aloft and small, lighter weight ice crystals ascend with the updraft. Supercooled water droplets must also be present as they have been experimentally proven to promote significant charge transfer (Reynolds et al., 1957). During collision, heavier graupel is typically negatively charged while the lighter ice crystal is positively charged (Reynolds et al., 1957). The outcome of the collision is illustrated in Figure 2.

The charge distribution that forms from this process within the cloud is depicted in Figure 3. This vertical tripole charge structure is primarily separated into several distinct regions of opposite charge. Depending on the thermal level at which the collisions occur, the charging of the hydrometeors can change. At lower temperatures, graupel pellets charge negatively. The opposite is true at higher temperatures. The temperature where this process changes is referred to as the reversal temperature and ranges from -10 °C to -20 °C at a height of approximately 6 km (Rakov, 2016).

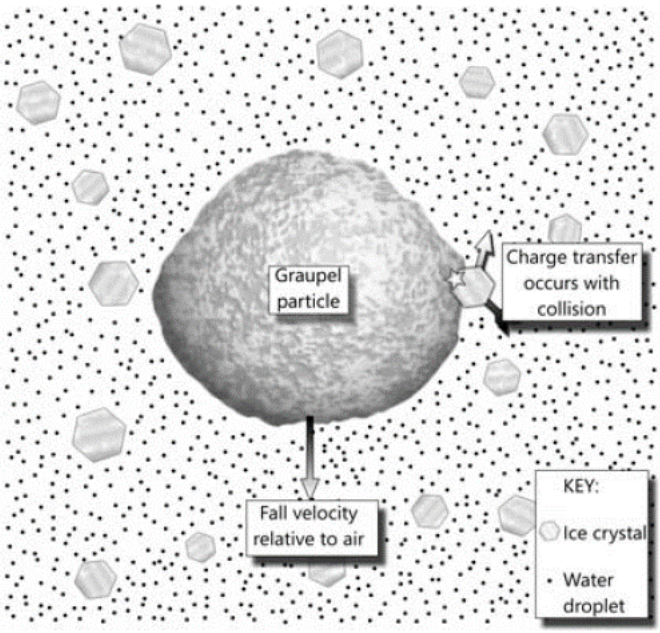

Figure 2. Schematic of the non-inductive charging mechanism illustrating the collision process between heavy graupel and a smaller ice crystal in the presence of supercooled water droplets. Image from Emersic (2006).

As a result of ice crystal and graupel collisions, the main negative charge zone exists between -10°C and -25°C and is bounded by two positive regions near the cloud base and the cloud top (Rakov, 2016). The mean height of this main charging zone is -15°C (Reynolds et al., 1957). Research conducted to determine the exact location of this negative charge zone has shown that it is dependent upon numerous factors such as ice crystal dimension, particle relative velocity, chemical impurities and liquid water content (Jayaratne et al., 1983). This negative charge region produces the most lightning and is almost always the source of cloud-to-ground lightning initiation (Wallace and Hobbs, 2006; MacGorman and Rust, 1998). Some positive polarity cloud-to-ground lightning does occur, typically from anvil lightning or from the upper part of the thunderstorm itself, but these are less than 5% of all cloud-to-ground lightning. Additionally, under some temperature and liquid water content conditions the charging is reversed, resulting in more frequent positive polarity cloud-to-ground lightning from the core of the thunderstorm (Roeder, 2018).

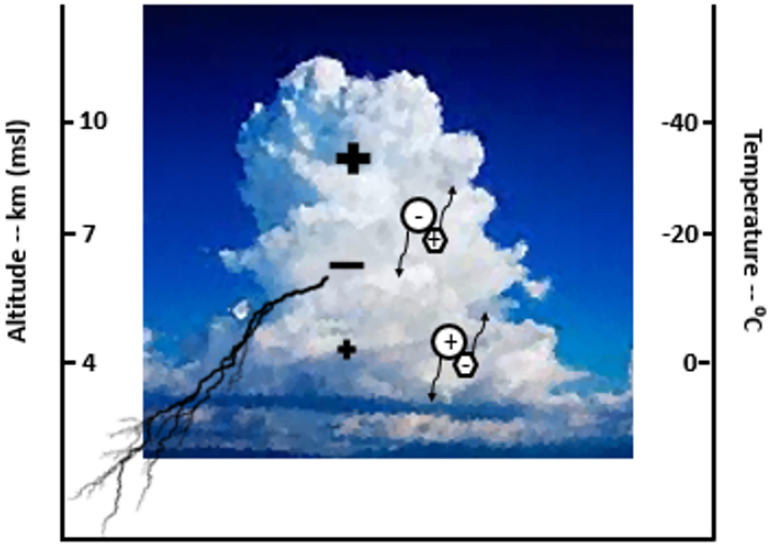

Figure 3. Charging of a thunderstorm causing the tripole charge distribution. As shown, graupel charges negatively at lower temperatures and positively at higher temperatures. Image adapted from Saunders (2008).

The positively charged region in the upper portion of the thunderstorm is a result of the upward flux of positively charged ice crystals. In contrast, the lower positive charged region of the thunderstorm could be a result of positively charged falling graupel resulting from collisions occurring below the reversal temperature (Wallace and Hobbs, 2006). The mixed-phase region occurs approximately between 0°C and -40°C and is the area in which graupel, supercooled water, and ice crystals coexist (Rakov, 2016). This region is also where the collision process occurs leading to charge separation within the cloud.

2.1.2 Lightning Discharge

If enough charge separation occurs, then the electric field might intensify to the point where dielectric breakdown occurs between charge regions in the cloud and/or between a charge region and the ground. More specifically, lightning occurs when the electric fields generated by a developing thunderstorm exceed approximately 3x10^6 Vm^{-1} (Rakov and Uman, 2003). This value is the field strength necessary for dielectric breakdown to occur in cloudy air at an altitude of about 6 km. This value can also vary depending on factors such as hydrometeor presence and the altitude at which dielectric breakdown occurs. Dielectric breakdown is defined as the rapid reduction in the resistance of an electrical insulator (in this case the cloudy air) when the voltage applied across it exceeds the breakdown voltage.

As a result of dielectric breakdown, an ionized channel is created through which charge can flow until no difference in electric potential remains (Wallace and Hobbs, 2006; MacGorman and Rust, 1998). This charge flow is essentially the lightning channel. It is also important to note that each individual storm cell exists with a considerably more complex charging structure than illustrated in Figure 3; however, this depiction adequately explains cloud electrification in a relatively simple

manner. Measurements from aircraft and balloon-borne field mills have shown that thunderstorm electric fields usually have a value of 3x10^5 Vm^{-1}, which is an order of magnitude less than the value needed for dielectric breakdown to occur (MacGorman and Rust, 1998; Roeder, 2018). This means that the large scale electric fields within a typical thunderstorm are too weak to initially cause the dielectric breakdown of cloudy air. This disparity has lead scientists to suggest that lightning initiates as a result of the emission of positive corona from the surfaces of particles of precipitation. The emission causes a local enhancement of the electric field which promotes the propagation of a corona streamer (Rakov and Uman, 2003). Ultimately, something else is taking place to help the initial dielectric breakdown start and this topic is currently on the cutting edge of lightning research (Roeder, 2018).

Typically, the ground is negatively charged, but as a thunderstorm moves through, the large negative charge region repels the negative charges on the ground, resulting in a positive area below the thunderstorm (NWS, 2017c). Cloud-to-ground lightning can be both positive or negative. Negative cloud-to-ground lightning (where negative charges flow from the cloud to the ground) is more common than positive and initiates from the main negative charge region to strike the positive ground below. When the less frequent positive cloud-to-ground strikes do occur, they are more dangerous (The National Severe Storms Laboratory, 2017). In addition to cloud-to-ground lightning, cloud-to-air, intra-cloud, and cloud-to-cloud lightning can also occur. There are also many variations of these lightning types such as a bolt from the blue, ribbon lightning, ball lightning, bead lightning and sheet lightning just to name a few. Of all the lightning types, intra-cloud lightning occurs the most frequently (The National Severe Storms Laboratory, 2017).

A flash of lightning is made up of two distinct parts: the initial dielectric breakdown discussed earlier and a stepped leader. A stepped leader is a negatively charged

plasma channel extending towards a region of opposite charge. The tip of the stepped leader does not sense the actual charges on the ground (for cloud-to-ground lightning). Instead, as it lowers the charge from the cloud it only senses charges within about 50 m of the leader tip. The stepped leader surges ahead in discrete steps based solely on the charges surrounding the tip of the leader (NWS, 2017c). As a result, the leader path from the cloud to ground is jagged and indirect. Therefore, the path that the stepped leader follows is not the path of least resistance as it moves blindly towards the ground (NWS, 2017c). The cause of this step-and-pause movement with specific step distances and time pauses is still not fully understood in the lightning community (Roeder, 2018). A typical stepped leader is 50 m long, but can range from 10-100 m, and lasts between 20-50 μs (Rakov and Uman, 2003). As the stepped leader approaches the ground, an upward leader forms in response to the large induced charge and increased electric field. The upward leader approaches carrying the opposite charge and meets the stepped leader approximately halfway (Roeder, 2018). The stepped leader then connects to a grounded object during the attachment process with the upward leader. The grounded object can be the ground itself, an object on the ground (i.e. a tree), or another region of opposing charge aloft (i.e. another cloud).

This attachment process is then proceeded by a return stroke which typically moves at 1/3 to 2/3 the speed of light (3.0×10^8 m/s). The return stroke is the flow of current through an ionized channel connecting the cloud and lightning termination point. It is also the brightest step of the lightning process (Rakov and Rachidi, 2009). A typical strike of lightning consists of the initial return stroke which is often followed by additional return strokes. These subsequent return strokes are generally initiated by dart leaders, which are related to stepped leaders except that they instead follow the pathway created by the initial return stroke (Rakov and Uman, 2003). The

number of return strokes in a flash is called the multiplicity of the flash. The average multiplicity is three to four, but there can be as few as one or as many as several tens of return strokes per flash (Roeder, 2018). Each of these steps are vital to the overall lightning discharge process.

2.2. Weather Radar

The weather radar is an important tool for meteorologists both in research and operational forecasting. Radar is a valuable and effective tool as it provides critical information about storm systems. Robust datasets collected by the radar can then be analyzed to further the understanding of weather concepts. This section provides a brief overview of the history of radar use in the field of meteorology. It also discusses the shift to dual-polarization radar. The section ends with an explanation of two dual-polarization parameters important to this study.

2.2.1 Weather Radar History

The details of the earliest origins of the use of Radio Detection and Ranging (radar) in meteorology are difficult to discern due to the secrecy surrounding this technology during World War II (WWII). At onset the of the war, the radio-location technology capabilities differed among the countries involved. On the British side, technology was more advanced largely due to the work done by Sir Robert Watson-Watt prior to WWII. By 1935, Watson-Watt was investigating the detection of aircraft using electromagnetic waves and his work ultimately laid the foundation for the first operational radar system (Whiton et al., 1998a). At the conclusion of WWII, the Weather Bureau (now known as the National Weather Service) received 25 radars previously utilized by Navy aircraft for operations during the war. Due to the S-band wavelengths of these radars, attenuation by rain was almost nonexistent (Atlas and

Banks, 1951), but accurate detection of snow and light rain was hindered due to system performance limitations. These radars were then modified for meteorological use and deployed at various locations across the country for operational use at a rate of approximately five per year.

The 1950s brought many improvements to both the weather radar capabilities for the military and also for the Weather Bureau (Whiton et al., 1998a). With the extensive damage caused by hurricanes in the mid-1950s, the Weather Bureau proposed a budget increase to aid in improvements for hurricane and tornado detection. Congress approved the budget and the Weather Bureau underwent extensive research to improve warning services. These efforts would eventually produce the flagship radar for the Weather Bureau, the Weather Surveillance Radars-1957 (WSR-57). The Weather Bureau chose an S-band wavelength for this radar in order to minimize attenuation occurring from rainfall. In 1970, the Weather Bureau had changed its name to the National Weather Service (NWS) and by the mid-1970s the NWS had received funding to replace older radars with 66 C-band radars known as Weather Surveillance Radars-1974 C-Band (WSR-74C) (Whiton et al., 1998a). The failure of seven WSR-57 radars between 1981 and 1985 and the desire to close five remaining gaps in radar coverage forced the NWS to purchase additional radars. In order to meet the criteria of hurricane and heavy precipitation detection, the NWS chose 16 Weather Surveillance Radars-1974 S-Band (WSR-74S) radars over the WSR-74C radars. The WSR-57 and WSR-74 were the first radars designed and built for the specific purpose of radar detection.

Depending on the purpose for the radar, different bands can be utilized. The S-band wavelength operates at a longer wavelength and is not easily attenuated, making it the preferred band for both near and far range observation of weather. Due to the longer wavelength, the S-band requires a large antenna dish and large motor to

generate power. In contrast, the C-band operates at a shorter wavelength and does not require a very large antenna dish or as much power for operation, making it the more affordable option. The drawback of the C-band wavelength is that it is more easily attenuated, making it difficult to discern hydrometeors radially behind heavy precipitation (Weather Edge, 2001; Roeder, 2018). Table 1 highlights the wavelength and frequency differences between the C-band and S-band.

Following the WSR-57, WSR-74C, and WSR-74S systems, researchers began developing radar technology that would incorporate the Doppler effect (Whiton et al., 1998b). This effect is the result of a moving wave source in which there is an apparent upward shift in frequency for observers towards whom the source is moving and an apparent downward shift in frequency for observers from whom the source is moving away. The result of this research was the Next Generation Weather Radar (NEXRAD) Weather Surveillance Radars-1988 Doppler (WSR-88D). Upgrading to a Doppler radar enabled meteorologists not only to see the location and intensity of the precipitation along with basic storm movement (as is the case for previous radar technology), but also the movement of the precipitation and winds within the storm. Simply put, the WSR-88D was the first radar with the capability to measure individual particle motion. Similar to previous radar systems, the WSR-88D operates on an S-band wavelength (Whiton et al., 1998b). After testing and development lasting through the 1980s, the first NEXRAD WSR-88D system was deployed operationally in 1992.

Currently, there are 160 WSR-88D radar locations across the United States and

Frequency Band	Frequency Range (GHz)	Wavelength Range (cm)
C	4-8	3.75-7.5
S	2-4	7.5-15

Table 1. Table adapted from the American Meteorological Society glossary highlighting the differences between the S-band and C-band radar wavelength bands.

overseas. The locations of these radars are shown in Figure 4. Each of these radars have a 10 cm wavelength and maximum range of 230 km. The WSR-88D operates by transmitting electromagnetic pulses with an average output power ranging from 300 watts to 1300 watts depending on the mode of operation (NWS, 2017b). It then measures the electromagnetic waves reflected back by both meteorological and non-meteorological targets to determine location, intensity, and movement of these targets.

The radar has two main modes of operation, precipitation mode and clear air mode. Precipitation mode is enabled when precipitation is expected and the radar completes a volume scan every 4-6 minutes depending on the Volume Coverage Pattern (VCP). A VCP is a series of 360-degree sweeps at specified elevation angles completed in a defined period of time (NOAA, 2017b). VCPs for precipitation mode are tailored for different types of precipitation and provide more elevation angles than clear air mode VCPs. More elevation angles result from the need of meteorologists to see higher in the atmosphere in order to analyze the vertical structure of the storms occurring. Figure 5 gives an example of a VCP activated in precipitation mode. Clear air mode is activated when precipitation is not anticipated, and one volume scan takes approximately 10 minutes to complete. An example of a clear air mode VCP is shown in Figure 6. The radar is also in its most sensitive operation state in this mode, which means it has the ability to detect smaller objects in the atmosphere. When precipitation is actively occurring, the radar does not need to be as sensitive as the rain provides plenty of returning signals (unlike in clear air mode).

Data from the WSR-88D radars are available through Level-II and Level-III datasets. Level-II is the base data given at normal resolution and it contains reflectivity, spectrum width, and mean radial velocity measurements. Base data also has the capability to produce derived products such as Vertically Integrated Liquid (VIL),

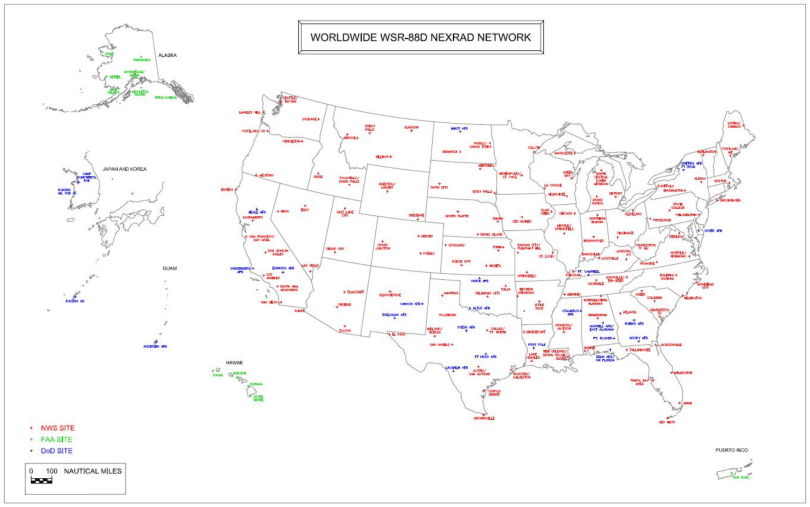

Figure 4. Map showing the worldwide NEXRAD WSR-88D network from the NWS Radar Operations Center (2017b).

storm total precipitation and various dual-polarization products (NWS, 2017b). All of the Level-II NEXRAD data are available through the National Centers for Environmental Information (NCEI) website. The files through NCEI typically contain four, five, six, or ten minutes of base data depending on which VCP the radar was operating in at the time of data collection (NOAA, 2017b). In contrast, Level-III data was developed to use less bandwidth and therefore has a lower resolution than Level-II data. Level-III datasets consist of 41 products made available as digital images directly from the NWS (NWS, 2017b).

There are between 50 to 100 Level-III products available intermittently through NCEI (NOAA, 2017b). A few of these products include hail estimates, echo tops, precipitation estimates, and storm relative velocity. Both the Level-II and Level-III

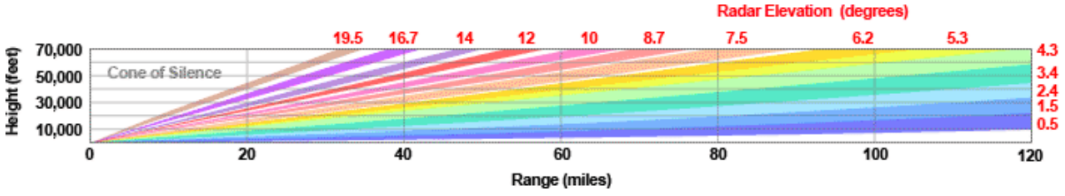

Figure 5. An example of the elevation angles utilized in one of the precipitation mode VCPs. Public domain image from NWS 2017b.

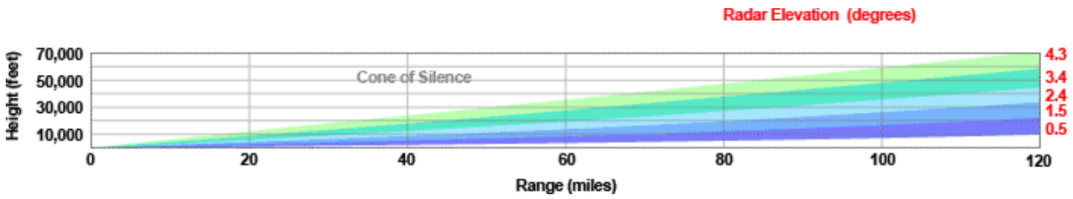

Figure 6. Graphic illustrating the elevation angles used in one of the clear air mode VCPs. Public domain image from NWS 2017b.

radar datasets are stored on a tape archive system and are accessible for a direct download or by placing orders for specific dates and times on the NCEI website. Once downloaded, data are typically received in 15 minutes or less. Occasionally, there are gaps and missing data in the archive. Scheduled maintenance at the radar sites, communications issues, archival problems and unplanned downtime as a result of severe weather are just a few of the reasons causing the gaps in data (NOAA, 2017b). The main NCEI data access web page provides a visualization of the file availability and the operating mode of the radar as an initial look at the weather for a given date.

2.2.2 Dual-Polarization Radar

Prior to February 2011, all WSR-88D radars only transmitted and received electromagnetic pulses with horizontal polarization only. This was done to receive the strongest reflected signal from large rain drops that tend to be wider horizontally than vertically (Roeder, 2018). By 2014, dual-polarization upgrades had been completed on over 150 NEXRAD radar sites (NWS, 2017b). Dual-polarization transmits and receives backscattered electromagnetic pulses with vertical polarization in addition to horizontal polarization as shown in Figure 7. This upgrade allows the radar to estimate both the horizontal and vertical dimensions of targets, which provides improvements on the size, shape, and diversity classification characteristics of hydrometeors. These characteristics allow for the ability to differentiate between var-

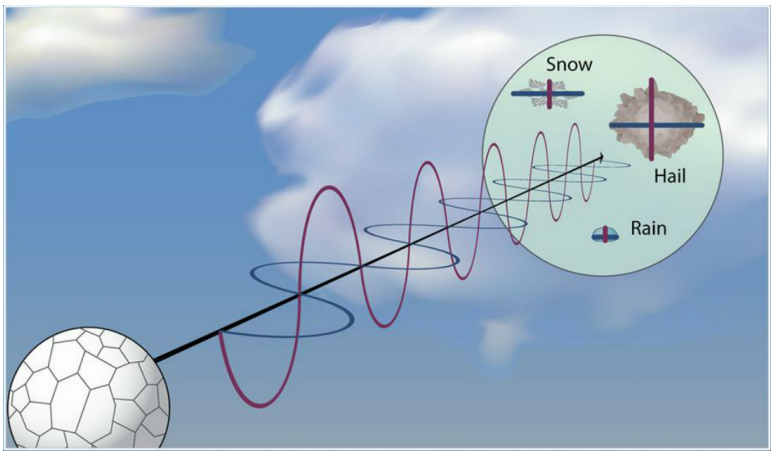

Figure 7. Depiction showing the horizontally (blue) and vertically (red) polarized waves emitted by a dual-polarization radar. The pulses hit targets (raindrops, snow crystals, and hail in this example) within the atmospheric volume covered by the pulse. Public domain image from NWS (2011).

ious hydrometeor types such as the snow, sleet, hail and rain depicted as targets in Figure 7. This upgrade improves the detection of non-meteorological targets such as ground clutter, chaff, birds, and tornado debris.

Dual-polarization also improves the accuracy of precipitation estimates which allows for more accurate flash flood detection. Improved flood forecasting was one of the main motivations for the NEXRAD dual-polarization upgrade as flooding is the leading source of storm deaths (Roeder, 2018). Identification of the melting layer through a bright band and detection of icing conditions for aircraft are additional examples of the improvements resulting from dual-polarization. Although the WSR-88D radars were only upgraded to include dual-polarization capability within the last five years, the theory and applications of polarimetric weather radar has been extensively researched for more than 30 years (Bringi and Chandrasekar, 2001).

2.2.3 Reflectivity

Reflectivity (Z) is a measure of the transmitted power returned to the radar, also known as the intensity. Z can be determined with radars that have horizontal

polarization only, therefore dual-polarization is not a requirement to obtain this parameter. The Z quantity is the most utilized WSR-88D product for both short-term weather forecasting and lightning initiation research. This usage is the result of the direct correlation between Z and precipitation intensity (Travis, 2015). A four panel example of Z is shown in Figure 8. The first step in determining reflectivity values is to calculate the power received by the radar from a target volume (Rinehart, 2010). Applying the Rayleigh assumption, the power equation is:

$$p_r = \frac{\pi^3 p_t g^2 \theta \phi ct \left|K\right|^2 lz}{1024 ln(2) \lambda^2 r^2} \tag{1}$$

where p_r is the power received by the radar, p_t is the transmitted power, g is the gain, θ and ϕ are the horizontal and vertical beam widths, ct is the speed of light (c) multiplied by the pulse duration (t). K gives the complex portion of the index of refraction, l represents attenuation, z is the radar reflectivity factor, λ is the wavelength, and r gives the distance from the radar (Rinehart, 2010). The Rayleigh assumption applies as the hydrometeors detected are typically much smaller than the transmitted wavelength of the radar. For a given radar, the p_t, g, θ, ϕ , t, and λ terms are constant parameters. A specific K value can also be designated with the assumption that the radar's main focus is liquid hydrometeors. Finally, the attenuation term, l, is also ignored as this quantity is often unknown. By combining all of the constants together into one value, the radar equation becomes:

$$p_r = \frac{c_2 z}{r^2} \tag{2}$$

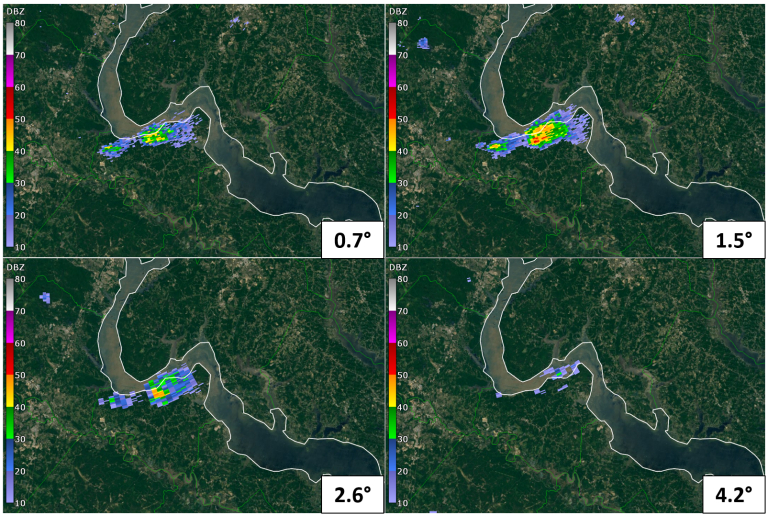

Figure 8. Four panel radar map showing four different elevation angles of base reflectivity. This image was created using the GR2Analyst software interface on 15 May 2012 at approximately 19:00:00 GMT.

where c_2 represents the grouped constants (Rinehart, 2010). The above equation can then be reorganized to solve for z:

$$z = c_2 p_r r^2 \tag{3}$$

which shows that the radar reflectivity factor is directly proportional to the range squared and the power received by the radar. In order to account for the variation of the particle sizes within a sample volume, another change must be made to the equation presented above. The sizes of particles detected by the radar can range from fog droplets (0.001 $mm^6 m^{-3}$) to large hail (36,000,000 $mm^6 m^{-3}$). A logarithmic radar reflectivity value of Z used to account for the range of values is given as:

$$Z = 10 log_{10} \frac{z}{1 mm^6 m^{-3}} \tag{4}$$

where Z is given in units of Decibels (dB) relative to $1 mm^6 m^{-3}$ (dBZ). This logarithmic adjustment causes Z values to range from approximately -30 dBZ for fog up

to 77 dBZ for very large hail (Rinehart, 2010). Both of the terms reflectivity and radar reflectivity refer to the term Z. An issue that arises with using reflectivity is determining if the large radar returns are a result of an increase in the size or number of hydrometeors. This has implications for flash flood forecasting as fewer large drops poses little flood threat while a very large number of smaller drops could be a flood threat (Roeder, 2018). Again, improved forecasting of flooding was the big motivation for the shift to dual-polarization which allows the forecaster to more accurately infer drop size.

2.2.4 Differential Reflectivity

Unlike Z, differential reflectivity (Z_{DR}) is a parameter only available with dual-polarization radars. It is calculated using the following equation:

$$Z_{DR} = 10log_{10}\frac{z_H}{z_V} \tag{5}$$

where z_H and z_V are horizontal and vertical polarization reflectivity factors, respectively (Rinehart, 2010). When Z values are measured logarithmically using Z_H and Z_V, the equation becomes:

$$Z_{DR} = Z_H - Z_V \tag{6}$$

where Z_{DR} has units of dB. With the inclusion of both horizontal and vertical axis information for a specific target, Z_{DR} provides important information for determining the hydrometeor shape. Z_{DR} measures the difference between horizontal and vertical reflectivity values. A four panel example of Z_{DR} is pictured in Figure 9 and a direct comparison of this figure with Figure 8 highlights the differences between Z and Z_{DR}. Both figures are from the same date and location.

Spherical targets will have identical values of z_H and z_V, which results in Z_{DR}

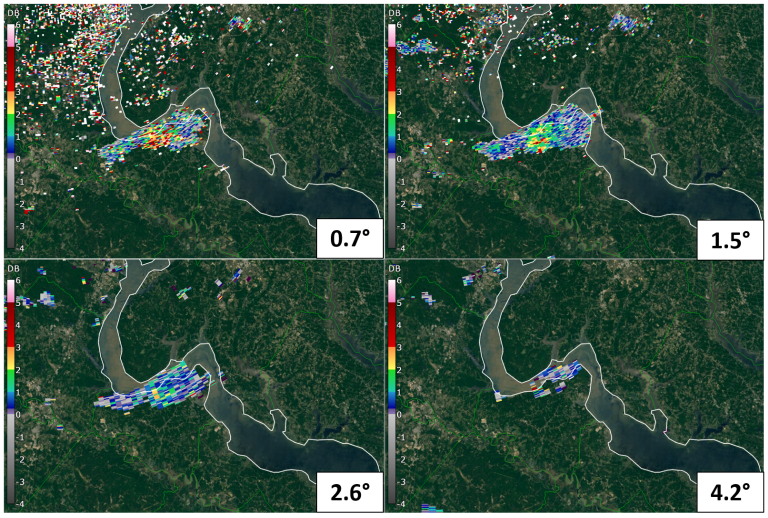

Figure 9. Four panel radar map showing four different elevation angles of differential reflectivity. The figure can be directly compared to Figure 8. This image was created using the GR2Analyst software interface on 15 May 2012 at approximately 19:00:00 GMT.

values near zero. Objects that are non-spherical will have either negative or positive Z_{DR} values depending on the z_H and z_V ratio. Positive Z_{DR} values indicate oblate or flat targets oriented horizontally (i.e. rain). In contrast, negative Z_{DR} values denote targets oriented vertically (such as ice crystals) (NWS, 2011). Figure 10 gives a table of typical Z_{DR} values for different objects found in the atmosphere. Values of Z_{DR} can also be enhanced by increasing the complex refractive index. A particles physical composition directly affects the complex refractive index, which is a measure of how reflective a particle is to electromagnetic radiation. For example, droplets of water, which have a higher complex refractive index than ice, will have higher Z_{DR} values than ice pellets of proportionate shape and size (Kumjian, 2013a).

For different types of hydrometeors, Z_{DR} values can differ substantially. As large raindrops fall, they experience the force of drag which causes them to spread horizontally. This process causes the larger raindrops to have higher Z_{DR} values than smaller drops, which do not encounter as much drag (Kumjian, 2013a). Z_{DR} values can also be helpful for determining intensity of rainfall as rainfall is typically heavier

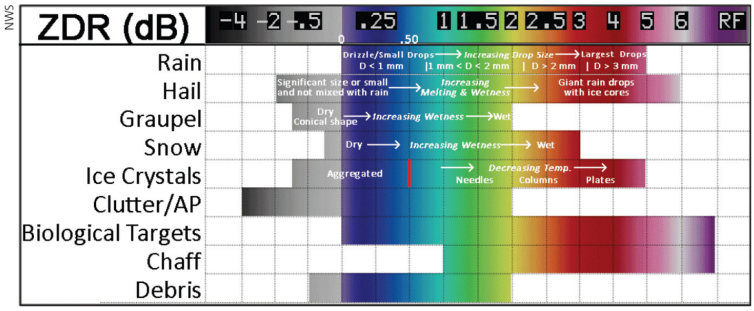

Figure 10. Typical values of differential reflectivity for various targets in the atmosphere as seen by the WSR-88D radar. Image courtesy of the NWS.

when larger drops are present. Although Z_{DR} is useful for estimating rain amounts, the values can drastically differ for graupel and hail as a result of hailstone shape and size variability. The majority of hailstones are spherical with Z_{DR} values near zero. Hailstones that are large enough ($\geq$ 5 cm in diameter) can even have negative Z_{DR} values. Although Z_{DR} values widely vary for hail, it can still be a useful tool for detecting large hail. One approach is to locate areas of near zero Z_{DR} values embedded in regions of high Z_{DR} values resulting from heavy rain. An additional method is to compare areas of high Z_H to regions of low Z_{DR} (Bringi et al., 1984). Overall, Z_{DR} is a useful forecast tool.

A Z_{DR} column is a column of enhanced Z_{DR} values (sometimes upwards of 3.0-4.0 dB) present above the freezing level within a convective cell. These Z_{DR} columns identify the region in convective updrafts where wet ice particles and supercooled water droplets are carried above the freezing level. This process plays a crucial role in cloud electrification as explained in a future section of this chapter. Z_{DR} columns are often present within the updraft maximum of ordinary convective cells and also along the edge of updraft maximums in supercell thunderstorms (Kumjian, 2013a). Due to the presence of Z_{DR} columns in ordinary convective cells, they can be used to determine when a cell has a sufficiently strong updraft coupled with mixed phase hydrometeors, such as graupel and supercooled water droplets which are necessary

for the cloud charging required prior to the initiation of lightning.

2.3. Lightning Detection

Several systems are available for the detection of lightning depending on the location of interest. For this particular study, a total lightning network known as the Lightning Mapping Array (LMA) is utilized. This section introduces the basics and the advantages of this lightning detection system.

2.3.1 Lightning Mapping Array

A LMA is a network of time-of-arrival geolocation sensors that passively receive very high frequency (VHF) impulses emitted as dielectric breakdown occurs within thunderstorms, especially the small fast components of a lightning flash such as stepped leaders (Wilson, 2005; Wiens, 2007; Thomas et al., 2004; Roeder, 2018). These sensors detect VHF radio waves associated with both cloud-to-ground lightning and lightning aloft. As the lightning channel develops, a map of the discharge path is produced, including channels within the cloud. VHF typically denotes radio waves with a frequency of about 30-300 MHz and a wavelength within the range of approximately 1-10 meters. Furthermore, hyperbolic shaped surfaces are utilized to pinpoint the exact locations of in-cloud lightning for this mapping array (Wilson, 2005).

More specifically, the time of arrival difference between a single pair of sensors provides a hyperbolic surface on which the discharge occurred. A second pair of sensors gives a second hyperbolic surface that intersects the first surface providing a 3-D curved line on which the discharge occurred. A third pair of sensors provides another hyperbolic surface intersecting the previous surfaces which typically yields two points on which the discharge occurred. A fourth pair of sensors provides an

additional independent hyperbolic surface which uniquely identifies the 3-D location of the discharge (Roeder, 2010). Figure 11 illustrates this process in both 2-D and 3-D. Since four sensors produce four pairs of time of arrival hyperbolic surfaces, this is the minimum number of required sensors to locate the stepped leader of a lightning flash in 3-D plus time. Operationally, more than four sensors are utilized to provide robust measurements to account for sensor outages, communication outages, and rejection of questionable locations via quality control algorithms (Roeder, 2018). Furthermore, the use of more than four sensors allows multiple candidate locations for a single discharge, which leads to improved location accuracy using statistical methods such as the chi-squared minimization. By connecting the stepped leader locations in space and time from the same flash, one knows the path of the lightning flash (Roeder, 2018, 2010).

LMAs have become widespread over the last decade throughout the United States and the typical configuration includes eight or more VHF receivers spread over a diameter of 50-100 km. Previous research has shown that the predicted flash detection efficiency exceeded 95% and the source detection efficiency exceeded 70% within a 100 km range of all networks (Chmielewski and Bruning, 2016). The time of the peak radiation event is recorded in every 80 μs window that a noise threshold is exceeded by a signal. This enables each station to detect up to 12,500 events, or triggers, per second, correlating to the number of 80 μs intervals in one second. For systems having 100 μs windows, the number of triggers is reduced to 10,000 events (Thomas et al., 2004). Although the strongest event in successive 80 or 100 μs windows has its time recorded, it is not uncommon for a local noise signal to exceed distant lightning signals in a given time window. Most of the local noise events are rejected through data processing because only events with similar arrival times at different stations indicate a common source.

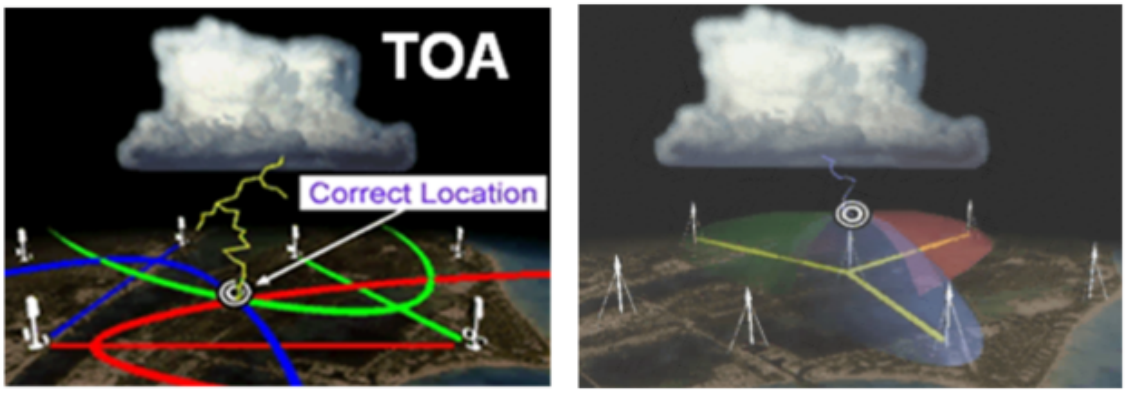

Figure 11. (a) 2-D (left) intersecting hyperbolae for a cloud-to-ground flash to determine the location of the return stroke. (b) 3-D (right) intersecting hyperbolic surfaces used to locate lightning aloft via time of arrival differences between pairs of sensors. Image from Roeder (2010).

A minimum of six stations is required to build a solution for the four unknowns (x, y, z, and t) of each event. This requirement provides at least two redundant measurements as a check on the solution's accuracy. Even with this rejection process, local noise events are still unavoidable in some solutions (Thomas et al., 2004). Processing for the LMA is done in one second segments and the arrival times at all stations within the network are sorted sequentially by time (Thomas et al., 2004). An example of how the LMA observes lightning in comparison to a cloud-to-ground sensor is shown in Figure 12. Overall, the LMA is able to provide more valuable information about the lightning strike than the cloud-to-ground network. Operationally, most meteorologists view the display of individual stepped leader locations and integrate the data into a flash visually (Roeder, 2018).

New Mexico Tech's LMA, located in Washington D.C., Alabama and Oklahoma, is a three-dimensional total lightning location system that was developed by Bill Rison, Paul Krehbiel, Ron Thomas and colleagues (Ramachandran, 2017). The LMA is modeled after the Lightning Detection and Ranging (LDAR) system developed by Carl Lennon, Launa Maier and colleagues at NASA's Kennedy Space Center (Rison

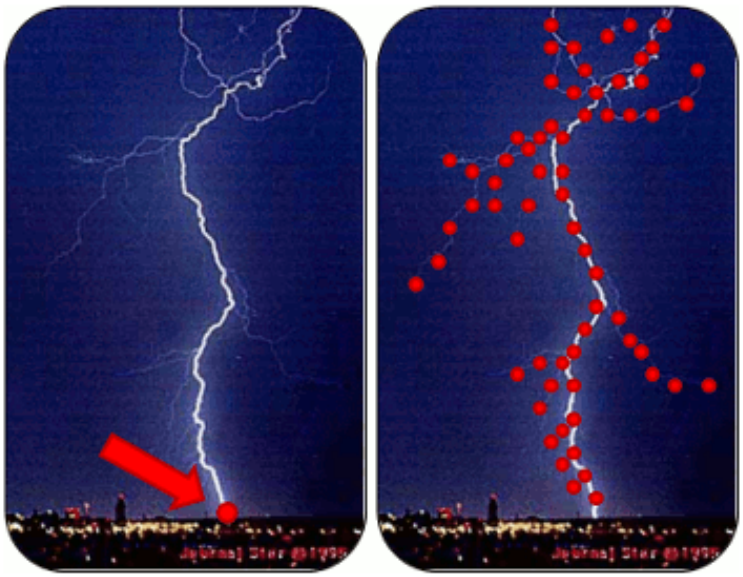

Figure 12. A comparison between what a total lightning network (LMA) observes with a lightning flash (right) versus what a cloud-to-ground network observes (left). It is important to note that the cloud-to-ground network only provides a single point of information (NASA, 2005).

et al., 2017). LDAR data has been previously utilized in lightning onset studies, most recently by Travis (2015). The signals for New Mexico Tech's LMA are received in an unused VHF television band, usually channel 3 (60-66 MHz) (Thomas et al., 2004). An example product for Washington D.C. is shown in Figure 13. Measurements taken at each of these stations are used to locate the sources of radiation to ultimately produce a three-dimensional map of total lightning activity in the D.C. area. This display provides the forecaster with a clearer picture of each lightning occurrence.

There are several advantages associated with using LMA data. First, the VHF source densities are updated frequently (every two minutes) as opposed to the longer volume scan (5 minutes) of radars. Second, cloud-to-ground lightning is preceded by in-cloud lightning by an average of about 5-10 minutes, allowing for a longer lead time for protective actions. It is important to note that the amount of time by which in-cloud lightning precedes cloud-to-ground varies considerably across the United States with a generally increasing trend from the southeast to the northwest.

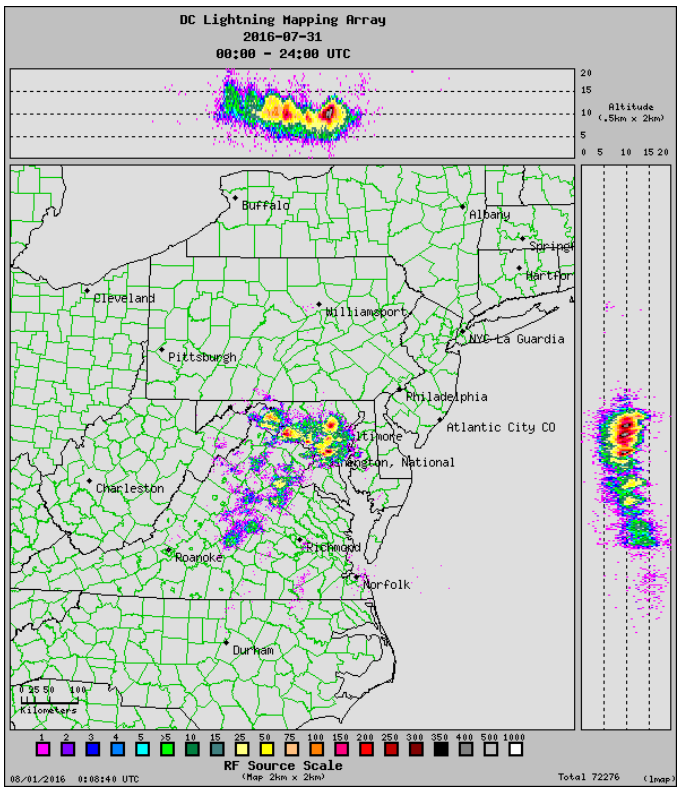

Figure 13. Product generated by the D.C. LMA on July 31, 2016 showing a three-dimensional map of total lightning activity within the area from Ramachandran (2017).

In Florida, the time difference is about 4 minutes while in Colorado it is closer to 20 minutes (Roeder, 2018). Third, research has shown that cloud lightning flash rates are highly correlated with the life cycle of a thunderstorm (initiation, development, and dissipation). Finally, VHF sources allow for a better approximation of storm echo top heights (Wilson, 2005).

2.4. Previous Research

Extensive research has been conducted in the field of lightning initiation; however, more work still needs to be done. This section introduces research conducted with reflectivity and lightning initiation. It then discusses studies conducted utilizing dual-polarization parameters to determine atmospheric conditions surrounding lightning initiation.

2.4.1 Reflectivity and Lightning

Many studies have been previously conducted relating lightning initiation to Z. The focus of these studies has been the amplification of Z values between the -10°C and -20°C thermal levels as this is the location of the main charging zone within a cloud. Amplified Z values within these levels indicates moderate levels of ice and graupel, which are necessary for cloud electrification. Most of the previous research obtained results comparable to the Pinder Principles which are conditions set to guide the forecaster's prediction of lightning onset and cessation for the 45WS. These principles were developed by Pinder in the early 1990s. During this time, he worked as a forecaster and Deputy Launch Weather Officer at the 45WS (Roeder and Pinder, 1998). Table 2 lists the Pinder Principles used by forecasters for lightning cessation and six different lightning onset scenarios. Forecasting each of these scenarios using the Pinder Principles relies on the use of weather radar. Since Roeder and Pinder (1998), the 45WS has stopped distinguishing between lightning aloft and cloud-to-ground lightning in issued lightning warnings. The distinction between the two types of lightning was difficult to do and the time difference between the events was too short for Florida (approximately 4 minutes) to be beneficial. Additionally, a significant minority (above 20%) of the deadly cloud-to-ground lightning occurred in under a minute after the first lightning aloft occurrence. It was ultimately deemed safer to forecast total lightning, especially lightning aloft, to provide customers a few extra minutes in which to take protective actions (Roeder, 2018).

In 1989, Dye et al. utilized aircraft, radar, and surface observations to analyze cloud electrification in New Mexico. The study found that the electric fields present within a convective cell did not exceed 1.0 kVm^{-1} until Z values exceeded 40.0 dBZ at the -10°C thermal level. The 1990 study by Buechler and Goodman yielded similar results. This study interrogated 20 thunderstorms located over Florida, New Mexico,

Phenomena	Lightning Type	Radar Intensity	Thermal Level	Vertical Depth
Convective Cell	In-Cloud	$37.0 - 44.0$ dBZ	$\geq -10°$C	≥ 3000 ft
Convective Cell	Cloud-to-Groud	$45.0 - 48.0$ dBZ	$\geq -10°$C	≥ 3000 ft
Anvil Cloud	In-Cloud	≥ 23.0 dBZ	$\geq -10°$C	≥ 3000 ft
Anvil Cloud	Cloud-to-Groud	≥ 34.0 dBZ	$\geq -10°$C	≥ 3000 ft
Debris Cloud	In-Cloud	$23.0 - 44.0$ dBZ	$\geq -10°$C	Variable
Debris Cloud	Cloud-to-Groud	$45.0 - 48.0$ dBZ	N/A	N/A
Cessation	All Types	When above conditions no longer exist.		

Table 2. Pinder Principles utilized for lightning onset and cessation using weather radar at the 45WS. Table adapted by Travis (2015) from Roeder and Pinder (1998).

and Alabama. They had a 1.0 Probability of Detection (POD) for the occurrence of lightning with a threshold of Z of at least 40.0 dBZ at the -10°C thermal level. Additionally, results of this study gave a False Alarm Ratio (FAR) of 0.20 and the lead times ranged from 4-33 minutes prior to lightning initiation.

The use of 40.0 dBZ at the -10°C thermal level prior to lightning initiation was also supported by several other studies including Gremillion and Orville (1999), Wolf (2006), Vincent et al. (2003), and Yang and King (2010). Research conducted by Wolf in 2006 was one of the largest studies as it analyzed more than 1160 convective cells in the Southern United States ranging from 2001-2006. The study aimed to provide real-time lightning alert information in order to better warn the public prior to the onset of dangerous lightning. Wolf's results highlighted that 40.0 dBZ at an updraft temperature of -10°C occurred prior to cloud-to-ground lightning initiation with a FAR of 0.11 and POD of 0.96. The updraft temperature used in the study was computed by plotting a parcel from the surface on a Skew-T/Log P diagram and then determining how high the -10°C thermal level would be within the violent updraft of a thunderstorm. This technique did not factor in the impact of environmental entrainment or vertical density differences. The value calculated at the updraft level will often be several hundred and upwards of several thousand feet higher than the environmental -10°C thermal level. Wolf (2006) concluded that probabilistic guidance

could be generated based on each scan of volumetric radar reflectivity data which leads to real-time lightning warning information.

Another larger study conducted by Yang and King (2010) analyzed a sample size of 143 thunderstorms. Yang and King analyzed thermal levels ranging from -10°C to -20°C coupled with Z values spanning from 30.0-40.0 dBZ. The purpose of this study was to determine the criteria that produced the most accurate results when predicting the initiation of cloud-to-ground lightning within airmass thunderstorms over Southern Ontario. Similar to prior studies, Yang and King (2010) concluded Z values of 40.0 dBZ located at the -10°C thermal level returned the best values of FAR and POD for the prediction of lightning initiation. Additionally, the study had an average lead time of 17 minutes. The results of this study uncovered the potential to develop a lightning nowcast algorithm suitable for Canadian forecast operational use.

Although the majority of studies concluded the best statistical results came as a result of Z values of 40.0 dBZ at the -10°C thermal level, alternative studies such as Mosier (2011) and Michimoto (1991) found that different thresholds gave the best results. Mosier (2011) objectively analyzed 67,384 unique convective cells. The cases spanned ten years (1997 through 2006) and were during the daytime in the summer located in Houston, Texas. WSR-88D radar data was used in conjunction with lightning data from the National Lightning Detection Network (NLDN). The convective cells were tracked using a modified version of the Storm Cell Identification and Tracking (SCIT) algorithm and then correlated to the NLDN data.

Mosier concluded that Z of 30.0 dBZ at the -15°C or -20°C levels were the best predictors of cloud-to-ground lightning based on statistics of the Critical Success Index (CSI). It is important to take into consideration that many of these studies analyzed cloud-to-ground lightning, which most often appears after the occurrence of intra-cloud lightning or cloud-to-cloud lightning. In fact, the LDAR system detected

lightning aloft an average of 5.26 minutes ahead of the occurrence of cloud-to-ground lightning in Forbes (1993). The analysis in this study also found several cases in which weaker convective cells only produced lightning aloft. The Pinder Principles shown in Table 2 require a lower Z threshold for the lightning aloft scenarios than for the cloud-to-ground lightning scenarios in order to account for these weaker thunderstorms that solely produce lightning aloft.

2.4.2 Dual-Polarization Parameters and Lightning

While prior studies have primarily focused on atmospheric conditions leading to lightning initiation, more work is needed to apply dual-polarization radar to this challenging problem. Parameters from a dual-polarization radar provide additional information about the structure and composition of a thunderstorm, which can be useful when determining the conditions necessary for lightning initiation. Research conducted by Hall et. al (1984) was some of the earliest work classifying hydrometeor type utilizing Z and Z_{DR}. Hall (1984) also noted building Z_{DR} values near the 0°C thermal level, which indicates the pulling of supercooled water droplets into a storm's updraft. This study showed that various hydrometeor types could be identified using the correlations between Z and Z_{DR} in a radar echo. The research also concluded that using Z alone would require considerable pattern recognition to make the same distinctions between hydrometeors.

One of the earliest studies of Z_{DR} columns was conducted by Illingworth et al. in 1987. They found narrow columns of positive Z_{DR} values to coincide with developing stages of cumulus convection. Illingworth et al. concluded that the Z_{DR} columns may be due to the large supercooled raindrops ascending in an updraft, and that the disappearance of the columns indicates rapid glaciation. While studying a multi-cellular thunderstorm in Florida, Bringi et al. (1997) found Z_{DR} columns indicating

regions of millimeter-size raindrops extending above the freezing level. These Z_{DR} columns were associated with the developing stages of each of the convective cells. The maximum values of Z_{DR} in this study ranged from 2.0-3.0 dB and extended from the 0°C thermal level up to the -10°C thermal level. Bringi et al. also observed that within a specific convective cell, the first intra-cloud lightning occurred within six minutes of mixed-phase conditions developing aloft. This process also corresponded to the Z_{DR} column diminishing. The use of Z_{DR} columns was thought to be potentially useful for the 45WS in providing a few extra minutes of lead time with issued lightning warnings (Roeder, 2018).

Shifting to the tropics, Carey and Rutledge (2000) also worked to develop methods to identify the occurrence of cloud electrification. Using a C-band dual-polarization radar, rain and ice masses were estimated during the entire life cycle of an electrically active tropical convective complex (known as Hector locally). The study showed that no significant lightning activity occurred during Hector's developing stages. In contrast, during the mature phase, lightning and the surface electric field were strongly correlated to the rainfall and mixed phase ice mass. Lightning activity again fell off during Hector's dissipating stages.

Research by Woodard (2011) and Woodard et al. (2012) utilized the dual-polarization upgrade to improve upon lightning initiation forecast methods that relied on Z alone. These studies relied on a C-band dual-polarization radar located in Alabama to analyze if Z paired with Z_{DR} led to statistical improvements of both intra-cloud and cloud-to-ground lightning forecasting. Woodard (2011) analyzed a total of 50 cases broken into 31 thunderstorm cases and 19 non-thunderstorm cases. The research concluded that the Z threshold of 40.0 dBZ at -10°C combined with Z_{DR} of at least 1.0 dB led to a 30 second improvement over the standard method of using solely 40.0 dBZ at -10°C. Additionally, the POD and FAR values were slightly lower,

which lead to an increase in the CSI. These results were not a statistically significant improvement of the forecast metrics or lead times. Particle Identification (PID) was also utilized by Woodard (2011) and allowed her to examine when the radar observed hail, graupel or supercooled water droplets. PID algorithms rely on fuzzy logic (truth values may be any real number between zero and one as a way to approximate human reasoning) and dual-polarization parameters in order to determine the probabilities of various types of hydrometeors existing within a radar volume scan. Utilizing the PID algorithm showed potential, especially when the algorithm identified graupel at the -15°C thermal level, but there are still assumptions and uncertainties hindering the use of the algorithm.

Similarly to Woodard (2011), Thurmond (2014) worked to improve upon the Z threshold of 40.0 dBZ at -10°C, but instead used a dataset of 68 convective cells over the KSC/CCAFS area in the summer months of 2012 and 2013. The research was conducted using the Melbourne, FL (KMLB) WSR-88D radar in conjunction with cloud-to-ground lightning data from the Marshall Space Flight Center website. Thurmond (2014) tested both Z_{DR} and specific differential phase (K_{DP}) thresholds. The analysis showed that K_{DP} did not show any added benefit, but Z_{DR} did lead to statistically significant improvements of the lightning initiation detection methods. For the analysis, Z values of 25.0, 30.0, 35.0, and 40.0 dBZ in conjunction with Z_{DR} values of 0.5, 1.0 and 1.5 dB were examined at the -10°C and -15°C thermal levels. The highest performing combination occurred with $Z \geq 30.0$ dBZ at -10°C paired with $Z_{DR} \geq 0.5$ dB. This method had a FAR of 0.24 along with a perfect POD of 1.0. These thresholds gave an average lead time of approximately 19.5 minutes which outperformed all methods relying solely on a Z threshold by at least three minutes.

The prior studies by Woodard (2011) and Thurmond (2014) show that dual-polarization radar can be utilized to identify the presence of hydrometeors necessary

for cloud charging. These studies also emphasized that a combination of Z and Z_{DR} predictors have the potential to improve forecast skill of lightning onset over methods that rely on Z alone. The most recent lightning initiation research, conducted by Travis in 2015, provided the basis for this study as he further describes the use of dual-polarization radar to improve lead times for lightning onset. More specifically, Travis (2015) built an initial dataset of 284 days with individual convective cells for a two year period ranging from March 2012 to March 2014. He analyzed both summer and winter season convection and utilized radar data from the KMLB radar. Travis (2015) relied heavily on the Four Dimensional Lightning Surveillance System (4DLSS) as it is the principal lightning detection system utilized by the 45 WS. This system detects lightning aloft data using the LDAR and cloud-to-ground lightning using the Cloud-to-Ground Lightning Surveillance System (CGLSS).

Travis created his initial database by subjectively selecting discrete convective cells when they appeared significant enough to produce lightning based on composite Z and size alone. The focus of his research was airmass thunderstorms. Consequently, days with complex areas or lines of thunderstorms tied to synoptic scale systems were not included in the analyzed database. This data was eliminated because within a larger complex of thunderstorms it is too difficult to relate the times of lightning initiation to an individual convective cell. Additionally, days with tropical cyclone activity were eliminated due to the banded nature of the convective cells. Convective cells located directly over the KSC/CCAFS/PAFB area were preferred, but any convective cells that were within a range of 100 km from the central LDAR antenna located at KSC were also recorded.

Travis downloaded radar data for all 284 days with discrete convective cells from the KMLB Level-II archives on the National Climatic Data Center (NCDC) NEXRAD Inventory. While downloading the data, if the radar was in clear air mode,

then the day was eliminated from the initial dataset. After days with radar outages, clear air mode VCPs, tropical activity, etc. were eliminated, 267 days remained in the initial dataset. Seven of the days had separate periods of convective activity in the morning and evening, so the final count of downloaded datasets was 274. To determine the height of the thermal levels utilized in the study, Travis relied on rawinsonde observations and the archived sounding data was obtained from the University of Wyoming.

For the analysis, Travis (2015) split the 274 time periods into training and validation datasets. To do this, he numbered the initial dataset from 1 to 274 with the odd numbers being incorporated into the training dataset. Travis created the training dataset as a majority of the previously conducted studies utilized cloud-to-ground lightning, so he wanted to determine the thresholds that would precede the initiation of all lightning types. The training dataset totaled 137 time periods and the individual convective cells were chosen using the Larsen area which is a region of significant radar reflectivity at a significant thermal level. For Travis' analysis, the cells were analyzed for a Larsen area defined by horizontal reflectivity threshold of greater than or equal to 30 dBZ at -5°C. Once a cell was identified for further investigation, Travis determined if the elevation angles of the KMLB radar intersected the thermal levels of interest (-5°C, -10°C, -15°C, -20°C) and cells that did not meet this criteria were eliminated. Discrete convective cells were finally incorporated into the training dataset when the VCP properly covered the four thermal levels of interest and archived 4DLSS data was readily available.

Travis analyzed a total of 125 discrete convective cells in the training dataset using Gibson Ridge Level 2 Radar Analyst (GR2Analyst) Version 2.13. The Z, Z_{DR}, and K_{DP} values were recorded for each of the cells at the four thermal levels of interest for a range of 0-50 minutes prior to lightning initiation or peak intensity.

Maximum Z values were also recorded when they occurred above one of the four thermal levels. Z_{DR} and K_{DP} values were again recorded within the updraft core containing the maximum Z value. The analysis of the training dataset produced 18 different predictors that could be compared with the lightning aloft predictors from the Pinder Principles. These 18 predictors utilized Z alone or Z coupled with other dual-polarization parameters at -5°C and -10°C.

After the training dataset analysis, Travis also conducted a validation set analysis. The validation set consisted of the remaining 137 time periods containing convective cells not analyzed in the training set. Each of these time periods was again analyzed using the same method as the training dataset time periods and narrowed down to 124 discrete convective cells. Travis then analyzed these cells to determine if they achieved any of the 18 thresholds developed by the training dataset. Hits, misses, false alarms, and correct rejections were then recorded. If the predictor threshold was exceeded by a cell and that cell produced lightning, then it was considered a hit. A false alarm was considered if the threshold was exceeded but lightning did not actually occur. Misses were recorded if the cell produced lightning but the predictor threshold was never met. A correct rejection occurred when the cell did not produce lightning and predictor threshold was not exceeded.

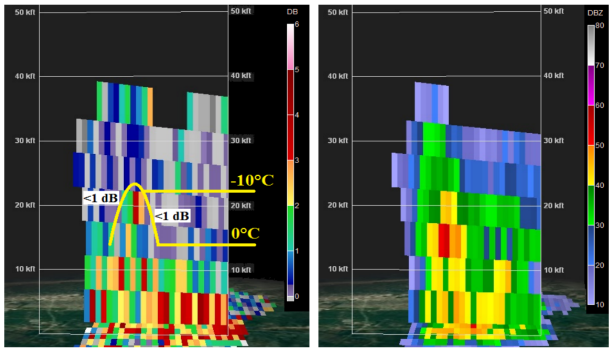

Figure 14. Vertical radar cross-section of an ordinary convective cell generated using GR2Analyst with Z_{DR} (left) and Z (right). A Z_{DR} column with values $\geq$ 1.0 dB extends above the freezing level within the main updraft core of the storm. Image from Travis (2015).

Travis (2015) highlighted that Z_{DR} is the preferred parameter to use in conjunction with Z values as elevated Z_{DR} values are indicative of supercooled water droplets and wet ice particles. More precisely, the mixed phase hydrometeors, which are necessary for cloud electrification, create a well-defined Z_{DR} column similar to Figure 14. The results of Travis (2015) confirmed that using both Z and Z_{DR} predictors increases the POD and lead time while decreasing the FAR. More specifically, Travis (2015) discovered two parameters, when used together, produced the best results: $Z \geq 36.5$ dBZ coupled with a $Z_{DR} \geq 0.31$ at the -10°C thermal level.

III. Methodology

This chapter will cover the steps taken during the analysis. It will also discuss the sources of the radar and lightning data used in the study. Then, an explanation of the rack-and-stack methods used to select the convective cells will be given. Finally, the steps taken to apply the Travis (2015) thresholds to the Washington, D.C. area will be explained.

3.1. Sources of Meteorological Data

The sources of the radar and lightning data are explained in this section. Specifics on the meteorological data in the Washington, D.C. area are also given in addition to the process behind retrieving the data for analysis.

3.1.1 Radar Data

Three weather radars provide coverage of the Washington, D.C. area. The Sterling, VA (KLWX) radar located approximately 25 miles northwest of Washington, D.C., the Dover Air Force Base, DE (KDOX) radar located approximately 110 miles east of Washington, D.C. and the Wakefield, VA (KAKQ) radar located approximately 138 miles southeast of the Washington, D.C. area. Each of these radars are shown in Figure 15. For this study, radar data was pulled exclusively from the KLWX radar as it provided optimal coverage of all thunderstorm cases analyzed. Archived Level-II radar data from the KLWX radar was downloaded from the NCEI (formerly NCDC) NEXRAD Data Inventory (NCEI, 2017).

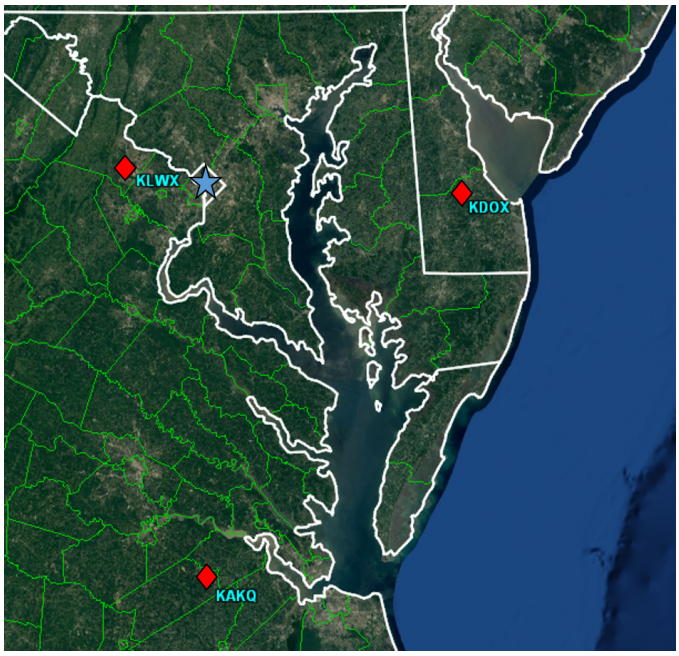

Figure 15. Map showing the locations of the three WSR-88D dual-polarization radar locations providing coverage of the Washington, D.C. area. The radar locations KLWX, KDOX, and KAKQ are denoted with red diamonds while Washington, D.C. is marked by the blue star. Generated using GR2Analyst.

3.1.2 Lightning Data

Although this study builds upon the work of Travis (2015), a different dataset will be utilized for lightning detection. More specifically, the LMA will be used instead of the 4DLSS. The LMA network located in Washington, D.C. locates the total lightning activity within a thunderstorm using a network that consists of ten sensors in and around the D.C. metropolitan area as shown in Figure 16. The sensors in this particular network span a 70 x 100 km area. The Washington, D.C. LMA is a joint demonstration project involving the National Aeronautics and Space Administration (NASA), the National Oceanic and Atmospheric Administration (NOAA), and New Mexico Tech.

Archived LMA data was downloaded from the DC LMA Post-Processed Data Archive (NASA, 2017b). The lightning data are post-processed with information

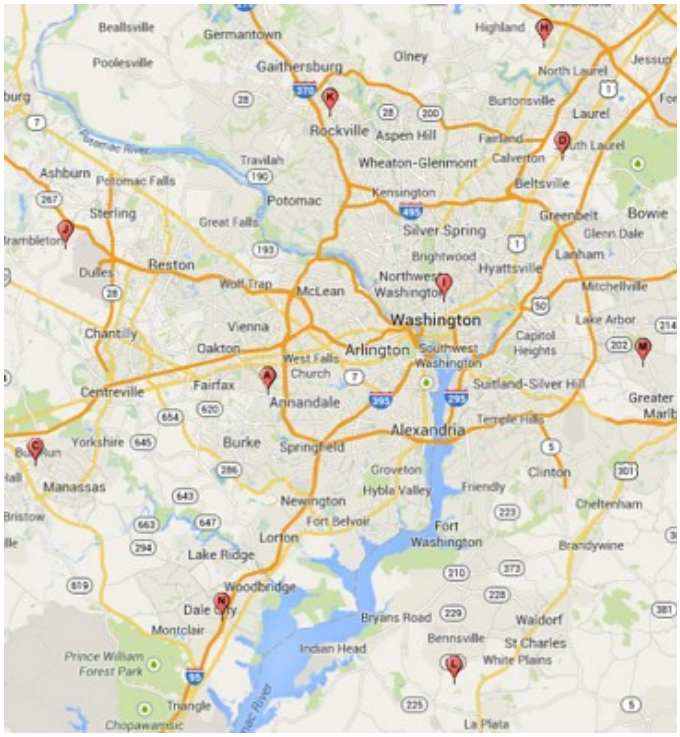

Figure 16. A Map showing the locations of the ten LMA sensors for the Washington, D.C. network. Image from NASA (2017a).

aggregated every hour. Downloaded files come in a compressed .gz format that must be unzipped in order to be analyzed. Additionally, the DC LMA Real-Time Browse Archive allows for a quick-look of lightning activity in the form of daily and hourly summaries (NASA, 2017c). Lightning information from this archive is retrieved in a .png format for a visual overview of activity.

3.2. Convective Cell Selection

The initial dataset was gathered using the NOAA NCEI Interactive Radar Map Tool (NOAA, 2017a). This tool shows supplemental data supporting the NCEI Radar Archive. The Interactive Radar Map Tool relies on the Reflectivity Mosaics products and web services from the Iowa Environmental Mesonet (Iowa State University, 2017). Users have access to data spanning from 1995 to present in five-minute intervals for

one or more stations at varying altitudes. Raw data are unavailable for download and is only accessible as images on the map tool or directly from the Iowa Environmental Mesonet (Iowa State University, 2017). On average, the range of radar products is 230 km from the radar site; however, rough terrain (i.e. mountains) blocks the lowest elevation angles of the radar beam in various locations. Different map layers are available within the Interactive Radar Map Tool. These map layers show the maximum distance from the radar (230 km), in addition to maps derived from geospatial models. The derived maps determine areas where rough terrain blocks the lower sweeps of the radar beam. NOAA's Radar Operations Center executes this analysis to provide beam coverage availability at specified altitudes from the ground. Three layers given by the map tool are located at 4,000 (best coverage), 6,000 (better coverage), and 10,000 (fair coverage) feet above ground. The range rings for best (85 km), better (110 km) and fair (160 km) coverage are also calculated using the three height layers. A sample of the Interactive Radar Map Tool is shown in Figure 17.

An initial dataset of 230 convective cells was collected using a quick-look method to eliminate and retain cases on the NCEI Interactive Radar Map Tool. These cases all span a six year period from 2012-2017. Only warm-season (May-September) cases were considered. First, the case date was analyzed for convective features. If a case date was dominated by a large multicellular structure or a squall line, then it was not considered for analysis. This omission is due to the complexity in attributing lightning initiation times to a specific convective cell embedded in a larger system. After an isolated cell was found on the map tool, it was measured using the ruler feature to determine if it fell within an acceptable range of the radar and the center of the LMA network. Specific intensity criteria were not used when compiling the initial database with the Interactive Radar Map Tool as this tool does not allow the user to see exact Z values of specific cells. Cases that passed the initial dataset

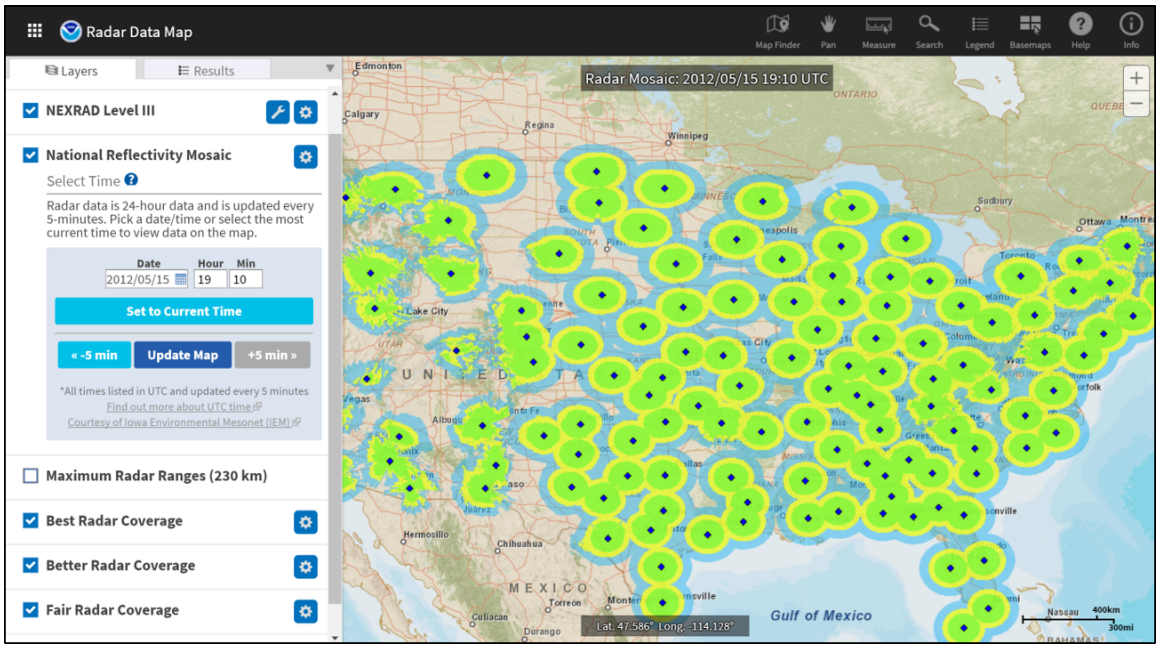

Figure 17. Sample image of the Interactive Radar Map Tool showing the best (green), better (yellow), and fair (blue) ranges for radars across the country. Spotty radar coverage is also evident over areas of rough terrain. Image from NOAA (2017a).

inspection were recorded in an Excel spreadsheet. The date, latitude/longitude, and start/end times along with any additional details (i.e. another storm passes over the area 20 minutes later) were also input into the initial dataset spreadsheet. A more restrictive rack-and-stack method was applied after the completion of the initial dataset collection process.

Using the GR2Analyst Version 2.60 software, the 230 convective cell initial dataset was narrowed down to a final dataset. GR2Analyst is an advanced NEXRAD Level-II analysis application that ingests raw Level-II radar data downloaded from the NCEI NEXRAD Data Inventory. Software users have the ability to produce cross-sections and high quality volumetric displays. The volumetric display feature creates quality isosurface and semi-transparent 3D displays for base Level-II products. GR2Analyst also includes several high resolution reflectivity-derived graphical products (Echo Tops, VIL, etc.) in addition to the standard Level II-data products. Dual-polarization radar products can also be viewed. The high resolution derived

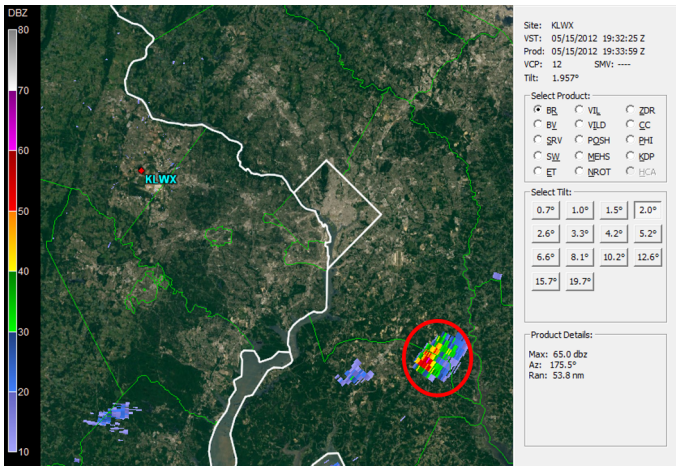

Figure 18. Example of a case used in the analysis as it met the set criteria for an isolated convective cell. Image generated using GR2Analyst.

products include five 2-D products all displayed on a high resolution radial grid. GR2Analyst can be used to view live radar data in addition to archived data. When the software is switched to Live mode, the products (both base and derived) update as a new volume scan is added. Purchase of a registration key is required to use GR2Analyst (GRLevelX, 2017).

Implementing a strict rack-and-stack method cut the initial dataset of 230 convective cells into a final dataset of 100 convective cell cases. Prior studies conducted by Woodard (2011), Thurmond (2014), and Travis (2015) utilized the Larsen area method of radar analysis and lightning initiation location (Larsen and Stansbury, 1974) to determine which cells to further investigate. The Larsen area is given as a region of significant radar reflectivity at a significant thermal level. For this study, the cells were analyzed for a Larsen area defined by a horizontal Z threshold $\geq$ 30 dBZ at -10°C. This Z value indicates substantial cellular development of a precipitation core based on the size distribution of hydrometeors associated with cloud electrification. The -10°C thermal level is significant to thunderstorm charge structure as it indicates the lower level of the main charging region and mixed phase region of the main negative charge zone.

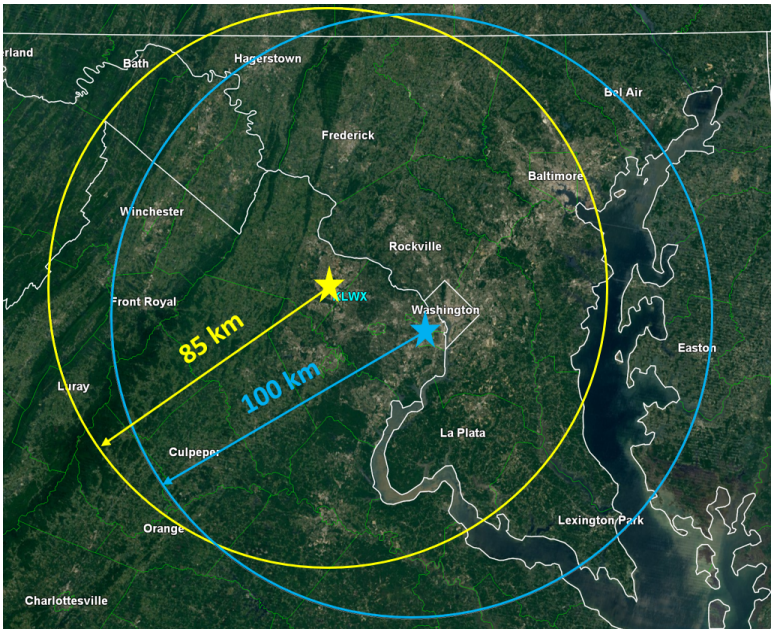

Figure 19. GR2Analyst map showing the KLWX radar range ring (yellow) and the Washington, D.C. LMA network range ring (blue) overlays. The stars denote the centers of the range rings.

Once the convective cell was determined to be significant enough to potentially produce lightning, the next step was to ensure it was isolated. The convective cell was considered isolated if there were no storms with connecting Z values greater than 15 dBZ (Patton, 2017). An example of an ideal isolated convective cell used in the analysis is shown in Figure 18. The next step is to verify that each of the individual convective cells fall within 85 km of the KLWX radar as NOAA defines this range as the range for optimal radar coverage (NOAA, 2017a). Cases must also be within 100 km of the center of the Washington, D.C. LMA network. This range was backed by a recent study, Chmielewski and Bruning (2016), that found the predicted flash detection efficiency exceeded 95% and the source detection efficiency exceeded 70% within 100 km of all LMA networks. Additionally, rough terrain to the west of Washington, D.C. negatively impacts the radar coverage just beyond this range. Placefiles for the radar and LMA network range rings were created using the WilmingtonWx Custom Range Ring Tools placefile generator (WilmingtonWx, 2017).

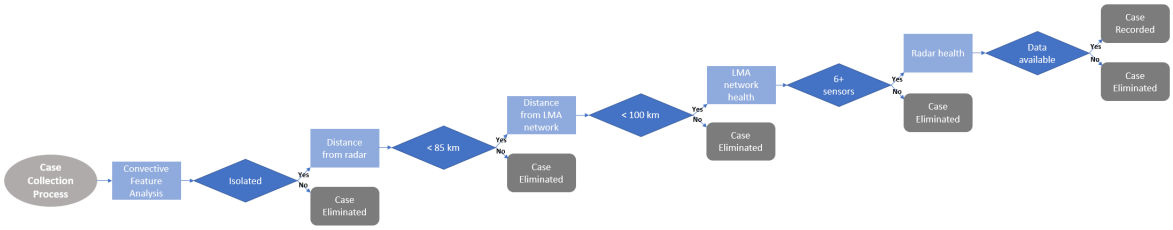

Figure 20. Flowchart illustrating the rack-and-stack method applied to build the 100 convective cell case final dataset.

Figure 19 shows the GR2Analyst map with both range ring overlays. Each of the convective cells must fall within the overlap of the two range rings to be considered for further analysis.

After verifying the location of the cases, the raw LMA data was read to determine the health of the Washington, D.C. LMA network. Six or more of the 10 sensors shown in Figure 16 must be operational to be considered healthy (Ramachandran, 2017). The final criteria of the case collection rack-and-stack method was to analyze the health of the KLWX radar. An overview of radar data availability for a specific date is provided by the NEXRAD Data Inventory (NCEI, 2017). A flowchart of the rack-and-stack method for case collection is given in Figure 20.

Additional reasons for case elimination included formation in the radar cone of silence or close enough to the radar where the beam angle is unable to view the -10°C height. Convective cells that formed over areas of spotty coverage to the west of KLWX were also eliminated. Finally, cells that merged with another cell or split into two cells early in their life cycle (prior to peak intensity) were cut from the dataset. After all of the requirements were applied, the initial dataset was dropped to a final dataset consisting of 100 individual convective cells used for the analysis of the lightning initiation criteria set in Travis (2015). The pertinent information for each of the cases was recorded in an Excel final dataset spreadsheet. An overview of the time of day and monthly breakdown of the 100 cases is shown in Figure 21. The

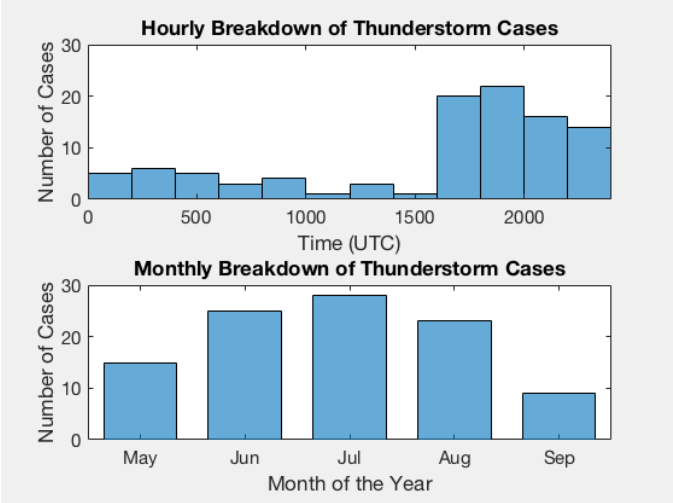

Figure 21. Histograms showing the time of day (top) and monthly (bottom) breakdown of the 100 cases from the final dataset. Image created using MATLAB.

majority of the cases occurred between 1600-2400 UTC (1200-2000 local time) with a peak at 1900 UTC and June through August.

3.3. Lightning Initiation Criteria Testing

After gathering cases in the final dataset for the analysis, both radar and LMA data were downloaded for the 100 convective cells. Specifics on how to obtain this data are covered in the Sources of Meteorological Data section. Prior to testing the Travis (2015) lightning initiation criteria, the LMA data were interrogated to determine whether or not a lightning strike occurred within each of the 100 convective cells. Specific latitude/longitude boxes and a time frame for each case was input into MATLAB code along with the ingested LMA data. Using "for loops", the code determined if there were any recorded lightning strikes at these specified times and locations. If MATLAB found that the strike does not exist, then the LMA hourly summary (similar to Figure 13) for the case was opened to verify that no strikes occurred at the specified location. In contrast, if MATLAB found that lightning initiation occurred, the "lati" and "loni" commands in MATLAB were utilized to

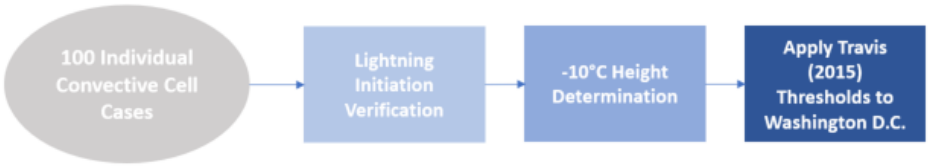

Figure 22. Flowchart illustrating the process of lightning initiation criteria testing after the convective cells have been gathered.

view the exact location of the lightning strike. This location was then verified using GR2Analyst to determine that the lightning is actually associated with the specified case rather than another storm passing through during the time frame. The final step of lightning initiation verification was to determine if the strike occurred within the core of the thunderstorm to eliminate the possibility of a bolt from the blue.

Following the verification of lightning initiation, heights of the -10°C thermal levels were collected for each case. Soundings provided by the University of Wyoming were utilized to determine the -10°C heights for the days encompassing the 100 convective cells (University of Wyoming, 2017). The -10°C height at 0Z and 12Z were recorded and then averaged to determine the -10°C height for a specific day. Soundings at 0Z and 12Z were the only times provided by the website for any given day.

Once the necessary steps were taken to build a complete and robust dataset, the analysis of the highest performing lightning initiation criteria from Travis (2015) over the Washington, D.C. area was conducted. A flowchart illustrating the process discussed is given in Figure 22. Previously, Travis (2015) developed a lightning initiation forecast method for use at CCAFS and KSC. At the -10°C height, $Z \geq 36.5$ dBZ coupled with $Z_{DR} \geq 0.31$ dB added the most utility to lightning initiation forecasts for these areas. To begin the analysis of these thresholds, radar data encompassing the time period for a single case was ingested into GR2Analyst. The case was located on the main base reflectivity interface, and the cross-section tool was then used to analyze a slice of the cell's base reflectivity. "Position" and "swing" controls

Event Forecast	Event Observed	
	Yes	No
Yes	Hit	False Alarm (FA)
No	Miss	Correct Rejection (CR)

Table 3. Summary of the possible forecast outcomes based on whether the event is forecasted and whether it is observed. Table developed by Travis (2015) from Jolliffe and Stephenson (2003).

within the cross-section tool allow the user to slide and rotate the slice in order to view the entirety of the convective cell. Time steps were advanced within the cross-section tool to provide access to the full life cycle of the convective cell. Hovering the mouse over individual pixels within the cross-section gives exact Z values, or the GR2Analyst dBZ legend can be referenced for approximate values. Heights were also clearly marked for easy reference within the cross-section tool.

This process allowed the user to determine if the $Z \geq 36.5$ dBZ threshold at -10°C was met at any point. The volumetric display function with an isosurface Z value set at 36.5 dBZ was also utilized to further verify that the Z threshold was met at -10°C. Using the volumetric display allowed for a 3D look at a set Z value for the entire convective cell, ultimately simplifying the process. The time that the Z threshold was met was recorded in the Excel analysis spreadsheet. If the threshold was never met, then "Does Not Exist (DNE)" was recorded for the case.

After the analysis of Z, the cross-section tool was again utilized to determine if the $Z_{DR} \geq 0.31$ threshold was met at -10°C. The same process of sliding and rotating the slices over all time steps for the convective cell was applied. Unlike Z verification, the volumetric display tool could not be used in the Z_{DR} analysis as this feature is only available for base Level-II products. The time (or DNE) was recorded when the Z_{DR} threshold was met. If both Z and Z_{DR} thresholds were met prior to lightning

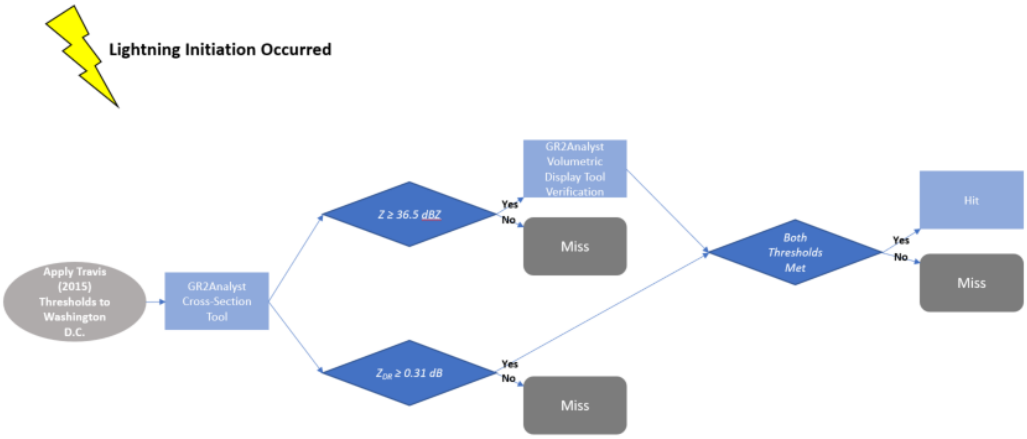

Figure 23. Flowchart illustrating the analysis process for lightning initiation criteria testing when lightning initiation has been confirmed.

initiation, then this time was recorded in the Excel analysis spreadsheet. The final step of the lightning initiation criteria testing analysis was to confirm if the thresholds' forecast matched with the lightning information collected from the LMA data (i.e. did the thresholds predict lightning and did a strike actually occur).

If the predictor threshold was met and the cell produced lightning, then it was recorded as a "hit". This scenario is illustrated in Figure 23. For each of the hits recorded, the volume scan time was marked as the hit time. The hit times were recorded to the nearest second and then subtracted from the time of actual lightning initiation (from the LMA data), providing the lead time for the threshold. If the threshold was met but the cell did not produce lightning, then a "false alarm" was recorded (Figure 24). If a cell did not reach the predictor threshold but still produced lightning, then it was marked as a "miss" (Figure 23). Cells that did not hit the predictor threshold and did not produce lightning were recorded as a "correct rejection" (Figure 24). A summary of the outcomes for the cells analyzed is given in Table 3. The lead time (if applicable) and whether the case was classified as a hit, miss, false alarm, or correct rejection was marked in the spreadsheet. Any additional

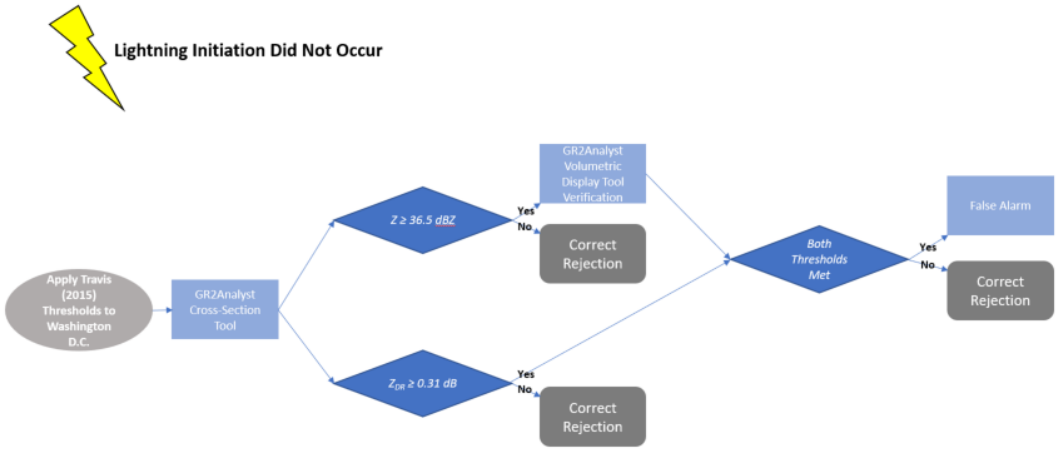

Figure 24. Flowchart illustrating the analysis process for lightning initiation criteria testing when lightning initiation did not occur.

details pertinent to the case were also recorded. This full analysis process was then repeated for the remaining 99 convective cells.

3.4. Forecast Metrics

Lead times and forecast outcomes were determined for each of the 100 individual convective cells from the final dataset. The performance of the lightning initiation predictor method was measured using forecast metrics utilized in Travis (2015). By using the same metrics, a direct comparison between the studies can be done. The Probability of Detection (POD) was the first metric tested. The POD is the hit rate and gives the proportion of correctly forecasted lightning occurrences (Jolliffe and Stephenson, 2003). It is defined as:

$$POD = \frac{Hit}{Hit + Miss} \tag{7}$$

where a POD near 1.0 is desired as it is indicative of a forecasting method that is limiting the number of missed forecasts. Although the POD provides useful informa-

tion, it is limited in measuring the overall skill of a forecast as it does not take false alarms into account.

In contrast, two of the metrics rely on the number of false alarms. The False Alarm Ratio (FAR) provides the probability of a false alarm when an occurrence is predicted (Jolliffe and Stephenson, 2003). The FAR is the same as the Probability of False Alarms (POFA) (Barnes et al., 2009), but will be referred to as the FAR for this study to remain consistent with Travis (2015) for an easier comparison. FAR is given as:

$$FAR = \frac{FA}{FA + Hit} \tag{8}$$

where a FAR near 0.0 is desired, and perfect skill is defined by a POD of 1.0 and FAR of 0.0. Similarly to POD, FAR is not a useful skill on its own due to the dependence on the amount of hits. The Probability of False Alarms (PFA) is another way to quantify the false alarms. This metric compares the false alarms with correct rejections (Jolliffe and Stephenson, 2003). This metric is also called the Probability of False Detection (POFD)(Barnes et al., 2009), but will be referred to as the PFA for consistency when comparing to the results of Travis (2015). PFA is defined as:

$$PFA = \frac{FA}{FA + CR} \tag{9}$$

where a value near 0.0 is ideal. This metric only provides limited insight into forecast reliability as it is dependent on correct rejections in the denominator.

The remaining forecast metrics provide valuable stand-alone information for measuring the reliability of a forecast. The True Skill Statistic (TSS), also referred to as Pierce's Skill Score, takes into account all of the statistics from Table 3. TSS

compares the PFA with POD in the equation:

$$TSS = \frac{(Hit * CR) - (FA * Miss)}{(Hit + Miss)(FA + CR)} \tag{10}$$

where the values can range between -1.0 and 1.0. A TSS of -1.0 indicates perfect skill with incorrect calibration while 0.0 means no skill (Jolliffe and Stephenson, 2003). A value of 1.0 is desired as it is indicative of perfect skill and correct calibration. TSS can serve as a reliable measure of accuracy as long as its threshold probability dependence is taken into account.

The final metric, Operational Utility Index (OUI), is a non-standard metric that was created by the 45WS to determine the operational utility of lightning forecast algorithms (Travis, 2015). OUI calculations combine the POD, TSS, PFA, and average lead time, in addition to a weighting scheme that reflects the operational priorities of the 45WS. The largest weight is assigned to POD as the ability to accurately detect lightning is vital to the safety of personnel. The next highest weight is assigned to TSS as it provides insight into the overall skill of a forecast method. PFA is given the lowest weight as the 45WS will accept some false alarms if a high POD is upheld. Lead time is also included in the calculation of OUI with an equal weighting to TSS. For this study, the average lead time for the forecasting algorithm is measured against the maximum lead time found through the analysis of the 100 individual convective cells. Travis (2015) used the OUI equation in his selection of the highest performing lightning initiation prediction algorithm as it optimizes standard forecast metrics. It is important to note that the OUI equation used in Travis (2015) was modified for this study to better normalize the lead time term. In this study the modified OUI equation is referred to as OUI*. OUI* is defined as:

$$OUI^* = \frac{(3 * POD) + (2 * TSS) + (2 * (\frac{LeadTime}{MaxLeadTime})) + (1 * (1 - PFA))}{8} \tag{11}$$

where LeadTime is the average lead time of a forecast algorithm and MaxLeadTime is the maximum lead time achieved by the same forecast algorithm for a given analysis. As previously mentioned, this equation is slightly different than the OUI equation used in Travis (2015) with the lead time term. MaxLeadTime was put in the denominator of the lead time term in place of the 30 minutes used in Travis (2015). Updated OUI* values calculated using the original dataset from Travis (2015) are provided in Chapter IV. An OUI* value of 1.0 indicates perfect performance while a score of 0.0 represents a useless performance by the forecasting algorithm. An overview of desired values for each of the forecast metrics is provided in Table 4.

3.5. Bootstrapping Method

Bootstrapping is a statistical technique that fits within the broader topic of resampling methods. The basic idea behind this technique is a relatively simple procedure that can be traced back at least two centuries, but the term "bootstrap" was coined and popularized by Bradley Efron in 1979 (Efron, 1979; Efron and Tibshirani, 1993). Although the process is not overly complex, it is repeated so many times that a computer must be utilized. As computing power improved and became less costly, the bootstrap techniques became more widespread (Taylor, 2017). For this study, MATLAB provided the means for applying the bootstrapping technique to the dataset.

Bootstrapping a sample performs calculations on the data itself to provide estimates of the variation of statistics that are computed from the same data (Orloff and Bloom, 2014). In a sense, the data is "pulling itself up by its bootstraps". The

Forecast Metric	POD	FAR	PFA	TSS	OUI*
Desired Value	1.0	0.0	0.0	1.0	1.0

Table 4. Overview of the optimal values for each of the forecast metrics.

term "bootstrapping" derives from the old phrase that "he lifts himself up by his bootstraps" which refers to an action that is irrational and absurd. No matter how valiant the attempt, no one can pick themselves up by pulling on tiny leather straps. This ties well to the bootstrapping technique as its application does feel impossible. It does not seem feasible that any improvements can be made on a statistic by using the same sample over and over again, but bootstrapping makes this possible (Orloff and Bloom, 2014; Taylor, 2017). This computer-based method is useful for assigning measures of accuracy to statistical estimates (Efron and Tibshirani, 1993). The bootstrap has a range of uses such as estimating standard errors and bias, determining confidence intervals, and even running tests (Hesterberg, 2015). The primary focus for this study was the generation of confidence intervals. In the case of lightning initiation forecasting algorithms, bootstrapping provides insight into the usefulness of the thresholds by quantifying the performance outcomes.

Bootstrapping may be easier understood when applied to an example. For this study, each of the convective cell cases from the original sample were assigned a number from 1 to 100. The case numbers were then randomly sampled with replacement 100 times to create a new set of 100 cases (called the bootstrap sample). Since replacement is allowed, the bootstrap sample will more than likely not be identical to the original sample. Some of the cases from the original sample may be excluded, while other cases may be duplicated in the bootstrap sample. Using the computational power of MATLAB, a total of 100,000 bootstrap samples were created by repeating this process in a relatively short amount of time. A statistical analysis was then run on each of these samples to generate the 95% confidence intervals. Figure 25 gives a visual representation of this example.

Although the bootstrapping 95th percentile method is a useful statistical technique, it is not the most accurate method for all datasets. The technique relies on

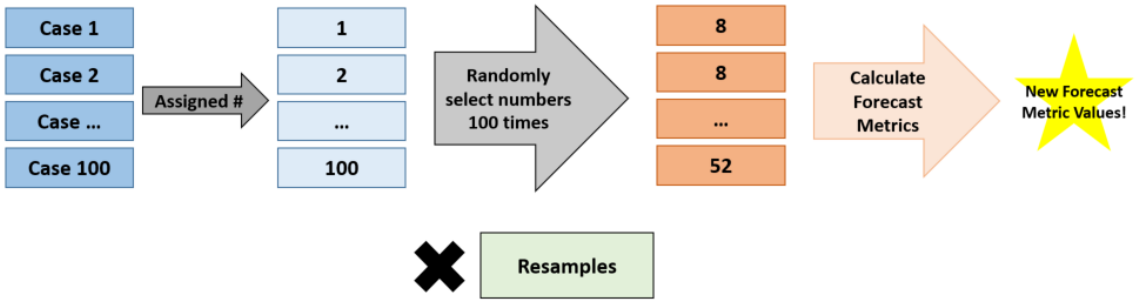

Figure 25. Flowchart illustrating the bootstrapping process used in this study. Each of the cases are assigned a number and then a new dataset of 100 cases is selected from these cases with replacement and omission allowed. Then, the forecast metrics are recalculated on the new bootstrap sample. This process is repeated based on the number of resamples.

obtaining sufficient data to have been reasonably well sampled. Small samples may not exhibit enough variability for bootstrap samples created from it to accurately represent the variability of the process that generated the original dataset (Wilks, 2011). Hesterberg (2015) gives the example of $n = 9$ for a small sample size and $n = 50$ for a large sample size and explains that for a quick estimation of standard errors or approximate confidence intervals, a resample size of 1,000 is sufficient. He also notes that when accuracy matters, a resample size of 10,000 or more should be utilized. For this study, the sample size is 100 isolated convective cells, which qualifies as a large sample size. Additionally, 100,000 resamples were used to produce the confidence intervals, so the bootstrapping technique is appropriate and provides accurate information.

IV. Analysis and Results

For this study, analysis of the lightning initiation prediction algorithm followed similar methods presented in Travis (2015). The main difference between this study and the Travis (2015) study was that this study applied the lightning initiation prediction algorithm to the Washington, D.C. area rather than in Florida for CCAFS/KSC. Travis (2015) also tested multiple predictors to determine if a combination of Z and dual-polarization parameters could be used to improve the skill over using Z alone for lightning initiation forecasts. Through his analysis, Travis (2015) concluded that two thresholds, when used together, provided the most skill for forecasting the initiation of lightning at CCAFS/KSC: $Z \geq 36.5$ dBZ and $Z_{DR} \geq 0.31$ at the -10°C thermal level. Instead of analyzing the performance of multiple predictors as in Travis (2015), this study determined the applicability of the top performing lightning prediction algorithm at a new location.

This chapter provides the results obtained from the analysis of the 100 individual convective cell cases using the Travis (2015) lightning initiation prediction algorithm. Additionally, a sample case is presented to show the steps taken to gather results. Finally, the chapter highlights the performance differences between the Travis (2015) study and this study utilizing the forecast metrics discussed in Chapter III.

4.1 Sample Case

In order to clearly represent the analysis conducted to obtain the results of this study, a sample case is given. The sample case analyzed is Case 1 from the final dataset. Case 1 is a convective cell that occurred on 15 May 2012 from approximately 1920-1950 UTC southeast of the KLWX radar. An image generated using the GR2Analyst interface showing the location of Case 1 is given in Figure 26. The

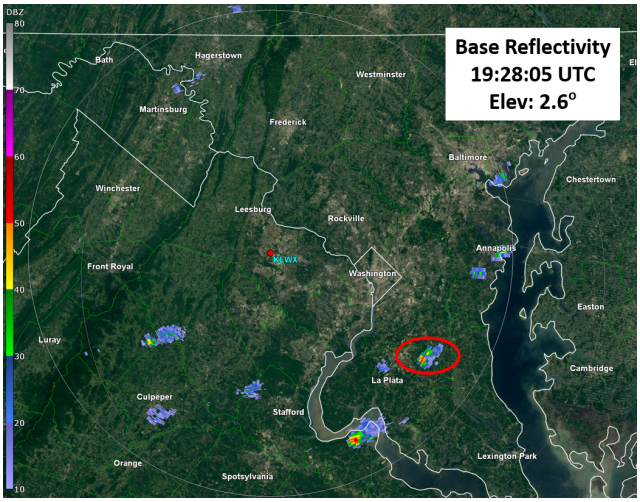

Figure 26. Radar image of the base reflectivity for Case 1 (red oval) used in the analysis. The image was from 19:28:05 UTC at an elevation angle of 2.6°.

-10°C thermal level for this case was 5170 m (approximately 17 kft) from atmospheric soundings provided by the University of Wyoming.

The first step was to use the GR2Analyst cross-section tool to determine if the $Z \geq 36.5$ dBZ at -10°C threshold was met. Figure 27a shows the cross-section created to analyze the Z threshold. A pixel exceeding 36.5 dBZ is shown circled in red above the -10°C thermal height at 19:28:05 UTC. To verify this finding, the volumetric display tool within GR2Analyst was utilized and is shown in Figure 27b. This 3D tool with an isosurface set for Z at 36.5 dBZ shows portions of the convective cell extending beyond the -10°C thermal height denoted by the red line. The volumetric display further supports the findings provided by the cross-section tool.

After the analysis of Z, the cross-section tool was again used to analyze if the $Z_{DR} \geq 0.31$ threshold was met at the -10°C thermal level. Figure 28 shows the cross-section created to analyze the Z_{DR} threshold. A pixel exceeding 0.31 dB is shown encased in the red circle above the -10°C thermal height at 19:23:47 UTC. The Z_{DR} threshold was met a little less than five minutes prior to the Z threshold, but 19:28:05 UTC was recorded for the time that the lightning prediction algorithm was fulfilled

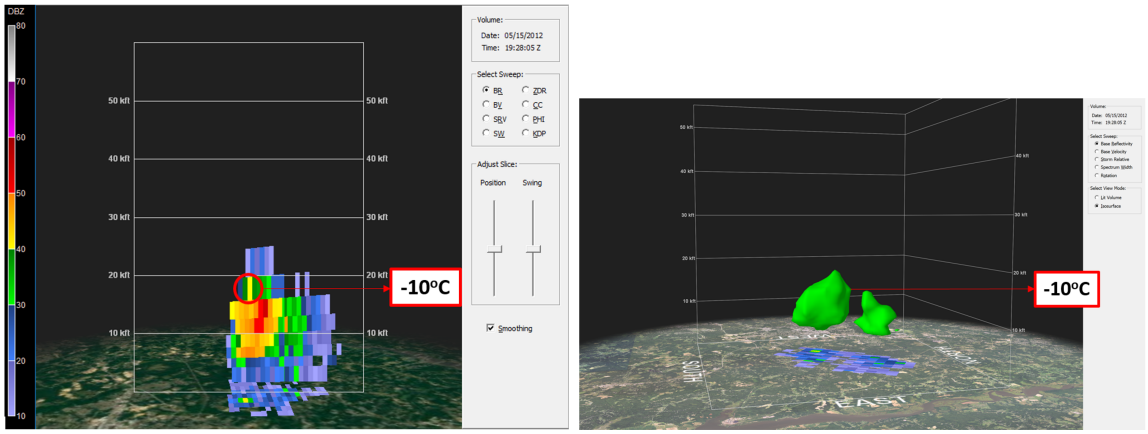

Figure 27. (a) Cross-section (left) of the Case 1 convective cell from 19:28:05 UTC on 15 May 2012. The -10°C thermal height for this case is denoted with a red line. The yellow pixel in the red circle indicates the area where the Z threshold was met. (b) Volumetric display (right) with an isosurface set at 36.5 dBZ for the Case 1 convective cell from 19:28:05 UTC on 15 May 2012. The -10°C thermal height for this case is denoted with a red line and Z values of 36.5 dBZ are shown extending above this height. This tool verifies with the cross-section tool that the Z threshold was met. Image generated using GR2Analyst.

as both predictors must be exceeded for the algorithm to work. Following the Z and Z_{DR} analysis in GR2Analyst, the LMA data was referenced to determine if lightning initiation occurred with the Case 1 convective cell. The MATLAB code created to ingest and read the large LMA data file for the case date found that no lightning was associated with the cell of interest. This finding was further verified with the hourly summary for the time period that the convective cell occurred. Although both thresholds from the lightning prediction algorithm were met in the analysis of this case, the overall outcome of Case 1 was a false alarm. Figure 24 simplifies the steps taken to obtain the results of this case analysis. The method explained for the sample case was then repeated 99 more times to generate a statistically significant dataset. Table 5 summarizes the breakdown of total cases within the dataset that had lightning occurring and provides the forecast outcomes for each of the cases after analysis.

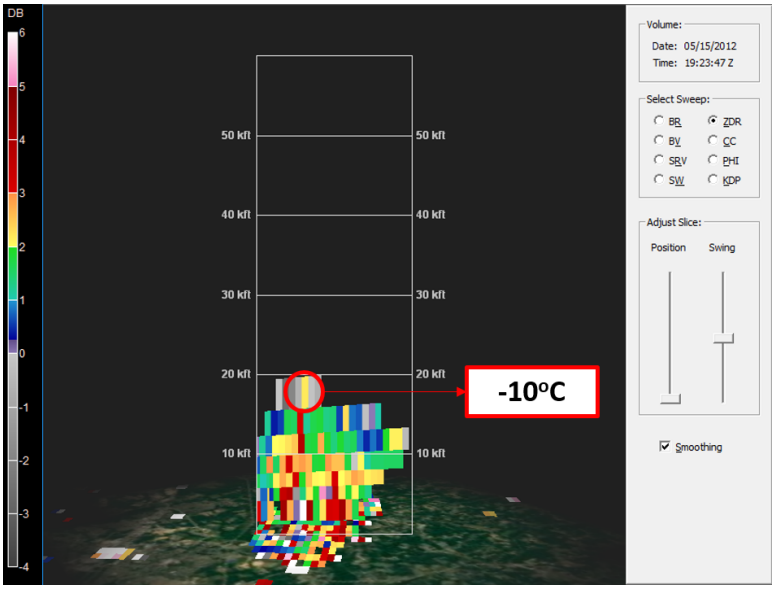

Figure 28. Cross-section of the Case 1 convective cell from 19:23:47 UTC on 15 May 2012. The -10°C thermal height for this case is denoted with a red line. The light yellow pixel within the red circle indicates the area where the Z_{DR} threshold was met. Image generated using GR2Analyst.

4.2 Travis (2015) Comparison

This section provides the comparison of the results from the Travis (2015) study to this study. It is divided into two subsections. The first gives the similarities and differences between the forecast metrics mentioned in Chapter III. The second provides the comparison between the lead times of both studies. Tables of values and graphics with the 95% confidence intervals are provided for a brief overview of the analysis results.

Lightning DNE	Lightning Occurs	Hit	Miss	CR	FA	Total Cases
65	35	26	10	38	26	100

Table 5. Summary of the 100 convective cell dataset that had measured lightning occurrences from the LMA data. The forecast outcomes for each of the cases are also given where CR is correct rejection and FA is false alarm.

4.2.1 Forecast Metrics Comparison

The comparison of forecast metrics calculated in Travis (2015) and this study highlights the applicability of the lightning initiation prediction algorithm when used in a new location. Table 6 summarizes the results of this comparison. The arrows indicate whether the metric for this study was above or below the metric calculated in Travis (2015). Each of the arrows are in red to indicate that the metric change showed a decrease in forecast skill. Table 4 provides the desired values for each of the forecast metrics to further highlight the values indicative of a skilled forecasting algorithm.

The first metric, POD, provides insight into the correctly forecasted lightning occurrences. For perfect skill, a value of 1.0 is needed. Travis (2015) had a POD of 0.8889 while this study had a lower value of 0.7222, indicating a higher hit rate for the lightning initiation prediction algorithm at the CCAFS/KSC than for the Washington, D.C. area. The next metric, FAR, gives the skill of a forecast based on false alarms. CCAFS/KSC had a FAR of 0.0588 while Washington, D.C. had a value that was almost ten times higher at 0.5000. The optimal value for FAR is 0.0, so the performance of the lightning initiation prediction algorithm based on this metric was much worse for the Washington, D.C. area. Table 5 shows that over a quarter of the cases resulted in a false alarm, contributing to the high FAR value. The PFA is another way to quantify skill based on false alarms. CCAFS/KSC had a PFA of 0.0769 while Washington, D.C. had a value over five times higher at 0.4063. The high value can again be attributed to the number of false alarms resulting in the analysis of this study. A PFA of 0.0 is optimal, so the lightning prediction algorithm showed less skill with this metric in the Washington, D.C. area. The final standard metric, TSS, accounts for all possible forecast outcomes (hit, miss, false alarm, correct rejection). Travis (2015) had a TSS of 0.8120, while this study had a value that was less than

	Washington, D.C.	CCAFS/KSC
POD	0.7222 ↓	0.8889
FAR	0.5000 ↑	0.0588
PFA	0.4063 ↑	0.0769
TSS	0.3160 ↓	0.8120
Mean OUI*	0.5108 ↓	0.7111
Median OUI*	0.4849 ↓	0.6848

Table 6. Table summarizing the results for the Washington, D.C. analysis of the lightning initiation prediction algorithm compared to CCAFS/KSC. The red arrows indicate whether the metric is higher or lower for Washington, D.C. than it was for CCAFS/KSC.

half that value of 0.3160. A TSS value of 1.0 is desired as it indicates perfect skill, so the lightning prediction algorithm again performed worse for the Washington, D.C. area.

Figure 29 gives the 95% confidence intervals of four standard forecast metrics for Washington, D.C. and CCAFS/KSC. This graphic was created in MATLAB using the bootstrap technique with 100,000 resamples. The values from the original dataset are given by the closed circles. Results for CCAFS/KSC are in red while the results for Washington, D.C. are shown in blue. Travis (2015) did not include confidence intervals in his original study. The MATLAB code used for the bootstrapping technique in this study was recreated and applied to the Travis (2015) dataset in order to resample and generate the 95% confidence intervals for a more accurate comparison of the two studies. Figure 29 shows that the POD is the only metric with overlap for the two studies. The overlap indicates that the POD value for this study is comparable to the value of Travis (2015). The FAR in Figure 29 has a large gap of separation, TSS has separation, and PFA barely touches with no overlap. Although the POD

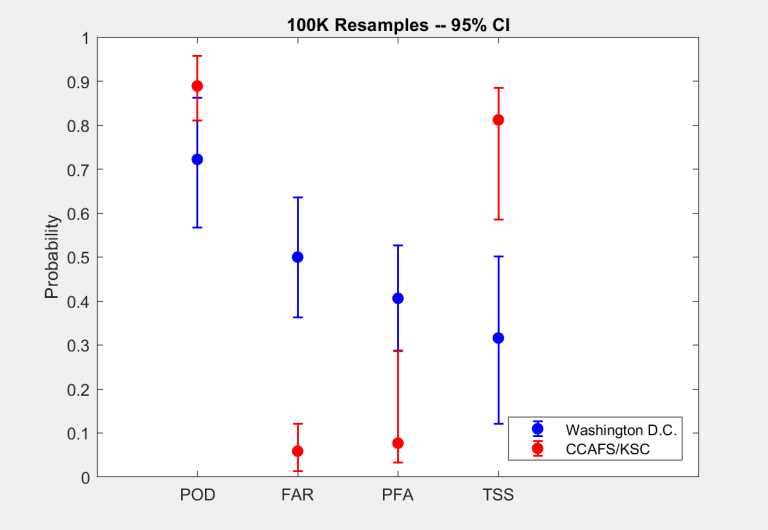

Figure 29. 95% confidence intervals of four standard forecast metrics (POD, FAR, PFA, TSS) for Washington, D.C. and CCAFS/KSC. The confidence intervals were created using the bootstrap technique with 100,000 resamples and values from the original sample, identified by the closed circles. The confidence interval shows that 95% of the time the values will fall within these error bars. Results for CCAFS/KSC are given in red and Washington, D.C. is in blue. Graphic created using MATLAB.

was not significantly different (due to overlapping error bars), it still matters that it was different. Figure 29 ultimately shows with confidence that the standard forecast metrics for this study are statistically different than those of Travis (2015).

In addition to standard forecast metrics, the non-standard metric, OUI, created by the 45WS was also analyzed. OUI provides insight into the operational utility of lightning initiation prediction algorithms. As the preferred metric of the 45WS, the lightning initiation prediction methods tested in Travis (2015) with an OUI closest to 1.0 were considered the best for operational forecasting purposes. The formula originally used to calculate OUI in Travis (2015) was updated for this study and is referred to as OUI*. Table 6 gives the mean and median OUI* values for both Washington, D.C. and CCAFS/KSC. More specifically, the 30 minute lead time used in the denominator of the lead time term was switched to MaxLeadTime in order to better normalize the term. Using the updated OUI* equation provided in Chapter III, the OUI* values were recalculated for Travis (2015) from his original dataset. The

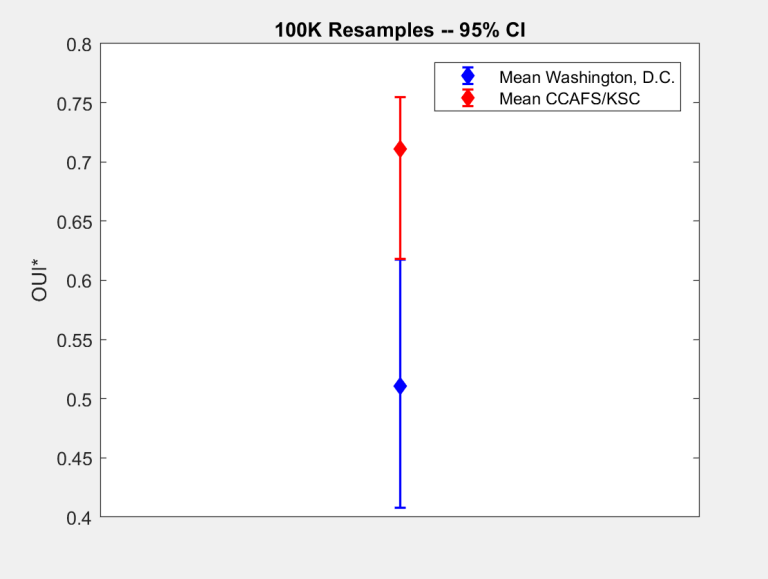

Figure 30. 95% confidence intervals of the mean OUI* for Travis (2015) and this study. The confidence intervals were created using the bootstrap technique with 100,000 resamples and values from the original sample, identified by the closed circles. It is important to note that the MATLAB bootstrap code used randomly samples the cases to generate new POD, TSS, and PFA values (in addition to lead times changing) for each OUI* resample to generate the OUI* plot. The confidence interval shows that 95% of the time the values will fall within these error bars. Results for CCAFS/KSC are given in red and Washington, D.C. in blue. Graphic created using MATLAB.

OUI* in this study was compared to the OUI* values from Travis (2015). Using the old equation, Travis (2015) reported a mean OUI of 0.7504 and median of 0.7067. The old OUI equation was also applied to the Washington, D.C. dataset and the mean and median values did not differ much from the values found using the corrected formula. Overall, using the old OUI equation from Travis (2015), the mean and median values for this study and Travis (2015) were only approximately 0.01-0.04 higher. With the updated and correctly normalized equation, Travis (2015) had a mean OUI* of 0.7111 and a median OUI* of 0.6848 while this study had a mean OUI* of 0.5108 and a median OUI* of 0.4849. The lower values found in Washington, D.C. indicate that the lightning initiation prediction algorithm had less operational skill at this location.

Figure 30 provides the 95% confidence intervals for the OUI* values in Washington, D.C. and CCAFS/KSC. Only the mean values are given and results for Travis

CCAFS/KSC are in red while the results for Washington, D.C. are shown in blue. Similarly to Figure 29, bootstrapping code with 100,000 resamples used in this study was tailored for the Travis (2015) dataset to create the 95% confidence intervals not originally provided in his study. The values from the original dataset sample are identified by the closed circles.

Figure 30 shows no overlap of the mean OUI* values for the two studies. Only the far edges of the 95% confidence intervals are near one another, indicating that the OUI* value found for Washington, D.C. is not statistically similar (no overlap) to the value for CCAFS/KSC. Assuming lead time and maximum lead time being equal, Washington, D.C. has the lower POD, lower TSS, and higher PFA which all act to lower the OUI*. The PFA for Washington, D.C. is much higher due to the high number of false alarms (26% of the dataset). This finding implies that the CCAFS/KSC thresholds are too easily met in the Washington, D.C. area and that the threshold for Z should be higher than 36.5 dBZ. Overall, none of the forecast metrics were close, so in terms of forecast metrics, the CCAFS/KSC lightning initiation prediction algorithm does not work well in the Washington, D.C. area which means that a single lightning initiation prediction method cannot be applied to the national NEXRAD network.

4.2.2 Lead Times Comparison

Along with forecast metrics, the comparison of lead times found in this study and Travis (2015) provides valuable insight into the performance of the lightning prediction algorithm at a new location. Table 7a provides the mean and median lead times (in minutes) for Washington, D.C. and CCAFS/KSC. The green arrows indicate that the lead times were higher in Washington, D.C. than for the CCAFS/KSC area. Table 7b provides the minimum and maximum lead times obtained through

	Washington, D.C.	CCAFS/KSC
Mean Lead Time (mins)	12.8462 ↑	11.8372
Median Lead Time (mins)	9.0000 ↑	6.6000

	Minimum Lead Time	Maximum Lead Time
Washington, D.C.	0 minutes	37 minutes

Table 7. (a) Table (left) summarizing the mean and median lead times for the Washington, D.C. analysis of the lightning prediction algorithm compared to CCAFS/KSC. The green arrows indicate whether the metric is higher or lower for this study than it was for Travis (2015). (b) Table (right) providing the range of lead times obtained for the 100 convective cells in the analysis of the Washington, D.C. area. These values were not provided in Travis (2015) and are therefore not included.

the lightning initiation prediction algorithm analysis for the Washington, D.C. area. These values were not provided in Travis (2015) for comparison and are therefore not included in the table. The lead times in Washington, D.C. spanned a wide range from 0 to 37 minutes for the 100 convective cell cases.

Figure 31a provides the 95% confidence intervals for the mean lead times and Figure 31b gives the 95% confidence intervals for median lead times reported by Travis (2015) and this study. The confidence intervals were generated with the bootstrap method using 100,000 resamples and the code was applied to the Travis (2015) dataset as the original study did not include confidence intervals for lead times. The values from the original dataset samples are denoted with the closed squares. CCAFS/KSC lead times are given in red while Washington, D.C. lead times are in blue. Figure 31a highlights that the mean lead times are statistically similar (indicated by significant overlap) and that Washington, D.C. had the superior lead times. The same result is shown in Figure 31b for the median lead times. The lead time confidence intervals span a much wider range in Washington, D.C. than for CCAFS/KSC. Overall, there is no significant difference between the mean and median lead times for Washington D.C. and CCAFS/KSC.

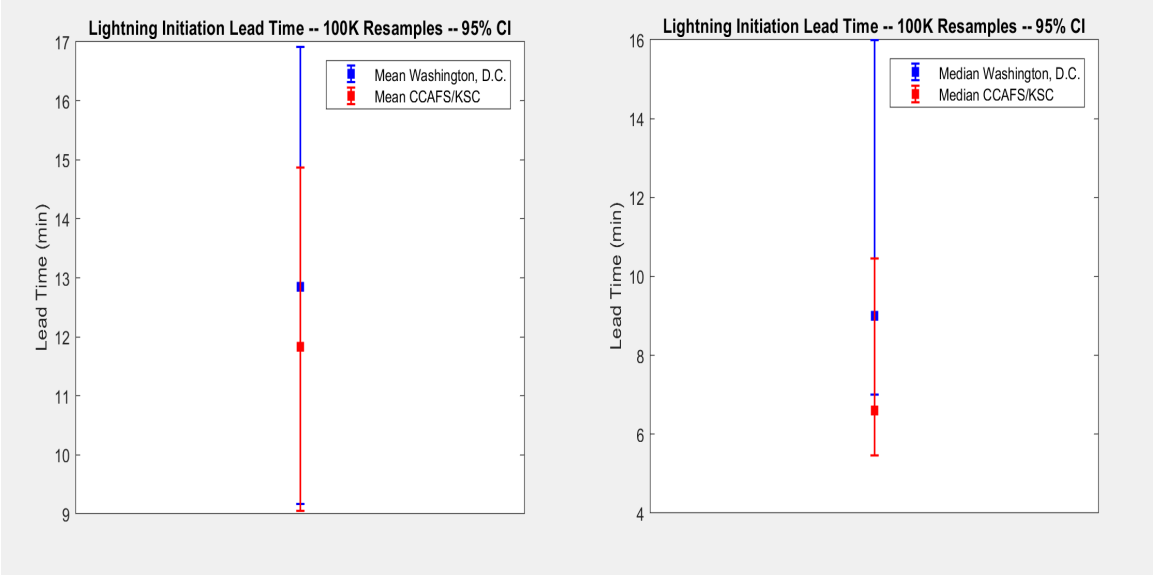

Figure 31. (a) 95% confidence intervals of the mean (left) and (b) median (right) lead times for Washington, D.C. and CCAFS/KSC. The confidence intervals were created using the bootstrap technique with 100,000 resamples and values from the original sample are denoted by the closed squares. The confidence interval shows that 95% of the time the values will fall within this interval. Results for CCAFS/KSC are given in red and Washington, D.C. in blue. Graphic created using MATLAB.

4.3 Additional Findings

While conducting the analysis of the Travis (2015) lightning initiation prediction algorithm over Washington, D.C., additional findings were made evident. For 53 out of the 100 convective cell cases, a Z_{DR} cell formed prior to the Z cell. An example of this occurrence is shown in Figure 32. Figure 32a was taken at 15:22:36 and has no Z signatures, only Z_{DR} signatures in the shape of a cell. Figure 32b was from four minutes later at 15:26:53 and Z returns are now evident. Both images are from an elevation angle of 8.1°. An explanation for the appearance of the Z_{DR} cells prior to Z cells could be the data displayed by GR2Analyst. The radar does not show below 10 dBZ on GR2Analyst (see the dBZ legend in Figure 32a and Figure 32b). This could have an impact because the equation for Z_{DR} subtracts the vertical Z (Z_V) from the horizontal Z (Z_H). If Z_H was 8 dBZ and Z_V was 2 dBZ, then GR2Analyst

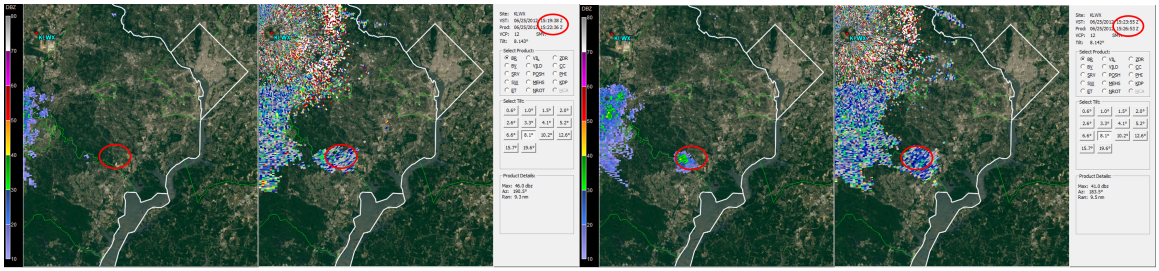

Figure 32. (a) Two panel radar display showing Z (left) and Z_{DR} (right) from 15:22:36 UTC on 25 June 2012. (b) Two panel radar display showing Z (left) and Z_{DR} (right) from 15:26:53 UTC on 25 June 2012. The red ovals on the map indicate the location of the convective cell. Image created using GR2Analyst.

would show Z_{DR} values but not Z returns on the screen. Additionally, these results are to be expected as supercooled water occurs first, then glaciation and the onset of electrification (Roeder, 2018).

The analysis for this study also found that for all cases the Z_{DR} threshold was met prior to or at the same time as the Z threshold. Three of the cases had the Z and Z_{DR} thresholds met at the same time and there were 10 cases in which both of the thresholds were never met by the convective cell. These results may indicate that Z_{DR} is not necessary as it is not a limiting factor (Z was the determining factor) for the Washington D.C. area. Simplicity is better for operational use by the forecaster, so utilizing only the Z threshold in Washington, D.C. could help expedite the lightning initiation forecast process.

V. Conclusions

Chapter V summarizes the outcomes of this study and provides insight into the potential reasoning behind various results. It also briefly covers the motivation and prior studies. Finally, this chapter explains additional research that can be conducted in the future to enhance and improve upon the findings of this study.

5.1 Summary

Lightning initiation is a danger to both life and property and has the potential to cause damage, injuries and even fatalities. Accurate forecasts of thunderstorms are vital for aviation, space launch, and overall public safety. The 45WS faces the difficult task of determining the most accurate lightning initiation prediction methods to protect over $20 billion in equipment, facilities and 25,000 personnel in and around CCAFS/KSC/PAFB (Travis, 2015). Although useful lightning initiation prediction algorithms exist for this area, these methods can be improved and possibly applied to new locations to increase the forecast accuracy of lightning nationwide.

Prior studies by Woodard (2011) and Thurmond (2014) determined that Z predictors, when used in conjunction with Z_{DR} predictors, improve the forecast skill over methods that relied on Z alone. Travis (2015) also confirmed that the implementation of dual-polarization added skill to lightning initiation forecasts. The highest performing lightning initiation prediction algorithm found by Travis (2015) was $Z \geq 36.5$ dBZ paired with $Z_{DR} \geq 0.31$ dB at the -10°C thermal level. The results of Travis (2015) showed that Z_{DR} is the preferred dual-polarization predictor to use with Z for the improvement of lightning initiation forecasts due to elevated Z_{DR} values indicating wet ice particles and supercooled water droplets. These mixed phase hydrometeors aid in cloud electrification within a developing updraft, and generate a Z_{DR} column

as discussed in Kumjian (2013b). It is important to note that the presence of a Z_{DR} column does not necessarily indicate the imminent onset of lightning, as most of the non-lightning producing convective cells that exceeded the -15°C thermal level in Travis (2015) also contained updrafts with an elevated Z_{DR} column.

Although Travis (2015) utilized the 4DLSS, the lightning data for this study was gathered from the Washington, D.C. LMA. Additionally, radar data was collected using the KLWX dual-polarization radar. This study investigated the applicability of the best performing lightning initiation prediction algorithm determined in Travis (2015). The method was tested on 100 isolated, warm season thunderstorms spanning six years in and around the Washington D.C. area. If the lightning initiation prediction algorithm verified well at this new location, it would build confidence for further use of the method at CCAFS/KSC and lend credence for use at other locations and eventual implementation as a new product in the NEXRAD network. This outcome would also benefit CCAFS/KSC since the WSR-88D in Melbourne, FL is used as their back-up weather radar.

At the conclusion of the analysis, this study found that the lightning initiation prediction algorithm used in Travis (2015) did not perform well when applied to the Washington, D.C. area. Figure 29 shows that the POD was the only forecast metric with a small portion of overlapping confidence intervals. The overlap indicates that the value of POD for this study is comparable to Travis (2015). Even though the POD was not significantly different (due to overlapping confidence intervals), it still matters that it was different from Travis (2015). Both FAR and TSS in Figure 29 have separation gaps between the confidence intervals, and PFA barely touches with no overlap. This figure concludes with confidence that the standard forecast metrics for Washington, D.C. are statistically different than those of CCAFS/KSC from Travis (2015).

For OUI*, Figure 30 depicts no overlap of the mean OUI* values for the two studies. The far edges of the 95% confidence intervals are near one another, indicating that the Washington, D.C. value is not statistically similar (no overlap present) to the value for CCAFS/KSC. If the lead time and maximum lead time are assumed equal, then Washington, D.C. has the lower POD, lower TSS, and higher PFA which all act to lower the overall OUI* value. The PFA found in Washington, D.C. is much higher as a result of the high number of false alarms (26% of the dataset). This finding implies that the Travis (2015) criteria for CCAFS/KSC is too easily met in the Washington, D.C. area and that the threshold for Z should be higher than 36.5 dBZ for the area. In terms of forecast metrics, the CCAFS/KSC lightning initiation prediction algorithm from Travis (2015) does not perform well for the Washington, D.C. area.

Although the forecast metrics were different for the two studies, the lead times were quite similar. Figure 31a gives the 95% confidence intervals for the mean lead times and Figure 31b gives the 95% confidence intervals for median lead times found by Travis (2015) and this study. These figures indicate that the mean and median lead times are statistically similar (indicated by significant overlap) and that Washington, D.C. had the slightly superior lead times. Ultimately, there is no significant statistical difference between the mean and median lead times reported in Washington D.C. and CCAFS/KSC. To the authors knowledge, no other studies have found these same forecast metric and lead time results.

The hope was that the lightning initiation thresholds would be similar for CCAFS/KSC and Washington, D.C. despite the different climates. The hypothesis was that using temperature as the vertical coordinate allows the physics to be the same. The heights of the electrification and charge separation occurrences will vary, but the temperatures will be the same. Therefore, one expects the same thresholds

for moisture, updraft, and cell volume to generate lightning, as long as temperature is used as the vertical coordinate (Roeder, 2017). The reasoning for different results in Washington, D.C. and CCAFS/KSC can be separated into two main categories: climate and equipment.

For climate, one explanation for the differences could be the role of aerosols in the electrification process and how this changes between differing climates. The Washington, D.C. area has a much greater population density than the CCAFS/KSC area according to data from the 2010 Census (United States Census Bureau, 2010). More people living in an area could be indicative of the production of more aerosols. Ice nuclei (aerosols) could facilitate more charge separation in the D.C. urban environment where more aerosols are present than the tropical environment found along the coast of Florida. Similar to this hypothesis, Yuan et al. (2011) found that increased aerosol loading over the West Pacific Ocean led to an increase in lightning activity through a modification of cloud microphysics. The results of this study could be related to the impact that aerosols have on lightning activity in Washington, D.C. versus the impact over CCAFS/KSC.

The differing forcing mechanisms present in Florida and Washington, D.C. could also provide insight into the lightning initiation prediction algorithm performance differences. In Florida, airmass thunderstorms are a common occurrence. These thunderstorms are relatively weak, short-lived storms and do not produce severe weather as the associated wind shear is weak. The main threats from airmass thunderstorms are periods of brief heavy rain and lightning. Airmass thunderstorms tend to occur within a maritime tropical air mass. The associated instability and lifting mechanisms are generally weaker. The Convective Available Potential Energy (CAPE) for severe thunderstorms is often more than double the values for airmass thunderstorms. Additionally, severe thunderstorms may have lifting from a strong approaching cold

front while sea breezes along Florida's coast are a common cause of airmass thunderstorms (Ahrens, 2014; Wallace and Hobbs, 2006). Sea breeze mechanisms are not present in the Washington, D.C. area as they are in Florida (Roeder, 2018).

Different forcing mechanisms for these two locations can be attributed to the different environments. Washington, D.C. is characterized as a baroclinic environment while Florida is more barotropic. Distinct air mass regions exist within baroclinic environments and fronts separate the warmer from colder air causing clear density gradients. Low pressure troughs (mid-latitude cyclones) and the polar jet can also be found in a baroclinic environment as this environment is typically located in the mid-latitudes. Simply put, the atmosphere is out of balance in a baroclinic environment (Ahrens, 2014; Wallace and Hobbs, 2006). In contrast, barotropic regions are characterized by a lack of fronts and uniform temperature distribution. The southeastern United States in the summer where each day brings about the same weather is the ideal example of a barotropic environment. Additionally, CCAFS/KSC has more maritime influence under either easterly or westerly flow while Washington, D.C. has a more continental influence under mainly westerly flow (Roeder, 2018).

Although the forecast metrics were quite different, the lead times found in this study and Travis (2015) were comparable. Figure 31a highlights that the mean lead times are statistically similar and that Washington, D.C. had the superior mean lead time by about a minute. Similar results are shown in Figure 31b for the median lead times. The lead time confidence intervals span a much wider range in Washington, D.C. than for Travis (2015). The longer lead times found in Washington, D.C. can be explained because thunderstorms develop for CCAFS/KSC/PAFB at a quicker rate due to strong instabilities (e.g. high CAPE values) in the area (Roeder, 2017). Even though Washington D.C. had larger mean and median values, the results were not significantly different and operationally these differences would not be significant

enough to really matter. Furthermore, when testing lightning initiation forecasting techniques in different locations, OUI* is the key metric for determining the utility of the method.

In addition to climate differences, equipment differences could have also impacted the results in the two locations. One possibility for varying results could stem from the lightning detection methods and associated lightning data. The Washington, D.C. LMA network may not be as sensitive as the lightning detection network located near CCAFS/KSC/PAFB. There were a few instances where a convective cell looked as though it should be producing lightning but the LMA was not reporting any activity. If this were the case, it could possibly explain the elevated false alarm rate found in the Washington, D.C. area. If the Washington, D.C. LMA network is not as sensitive, then it would not detect some lightning flashes when a flash has actually occurred, resulting in the case being classified as a false alarm. Additionally, different radars were used for the analysis in Travis (2015) and this study. This means that the radars could potentially be tuned differently from one another which may have led to bias.

The results of this study conclude that the lightning initiation prediction algorithm from Travis (2015) for CCAFS/KSC does not perform well for the Washington, D.C. area. This implies that one lightning initiation prediction algorithm cannot be applied across the entire national NEXRAD network. The lightning initiation prediction algorithm must be modified depending on climate or equipment.

5.2 Future Work

Although this study provided new insight into the difficult problem of forecasting lightning initiation, more work must be done to further investigate this challenging task. To increase the overall confidence level of this study, the convective cell dataset

could be expanded beyond 100 cases. For simplification of this study, which would allow for the analysis of more convective cells, the manual analysis process of using GR2Analyst could be automated. More specifically, a SCIT algorithm could be developed. This technique was utilized by Mosier et al. (2011) to analyze 67,384 unique convective cells. Information regarding the development of a SCIT algorithm is covered by Johnson et al. (1998). Similarly, Patton (2017) utilized the Warning Decision Support System-Integrated Information (WDSS-II) software to track storms based on user defined parameters such as composite reflectivity or a Hydrometeor Classification Algorithm (HCA) value. Some of the algorithms used in this software are based loosely on the WSR-88D SCIT algorithms. More information on the use of this algorithm can be found in Patton (2017). The time and coding skills required to ingest and analyze the LMA and dual-polarization radar data into these types of storm tracking algorithms extended beyond the scope of this study.

This study could also be expanded by incorporating dual-polarization radar data from some of the surrounding radars in the Washington, D.C. area. For this study, only the KLWX radar was utilized, but applying the analysis to different radars could yield interesting results. For example, someone could use the same 100 convective cells analyzed for this study with a different radar dataset to determine if the same results are found. This study could also be expanded by testing the lightning initiation prediction algorithm in different geographical locations such as the mountains, inland plains, desert, or Pacific Coast. When testing lightning initiation prediction methods in new locations it is important to note that OUI* should be the key metric used to determine the utility of a technique. Additionally, this study could be recreated using a different location's LMA network (e.g. Oklahoma, Alabama). This type of study would illustrate whether the lightning initiation prediction algorithm performs better in regions different than the Washington, D.C. area or if the algorithm is only

useful for Florida.

Further research could be conducted on this topic by including additional dual-polarization parameters, specifically Level-III products such as the HCA. Since the presence of graupel and ice particles are necessary to the cloud charging process, identification of these hydrometeors could be helpful for forecasting lightning initiation. An algorithm similar to the one used for lightning cessation in Patton (2017) could potentially be modified to create a new method for the prediction of lightning initiation. In addition to the inclusion of different dual-polarization parameters, the Z and Z_{DR} thresholds currently used could be adjusted and retested. This approach would help determine the optimal values for the Washington, D.C. area as the current thresholds are too low and were too easily met. If the original lightning initiation prediction algorithm from Travis (2015) were applied to new locations other than Washington, D.C., then based on performance outcomes the algorithm could be adjusted for these locations too.

The additional findings covered in Chapter IV of this study could be further developed for future work. This study showed that Z_{DR} may not be necessary when forecasting for Washington, D.C., so this could be analyzed to determine changes that would make the algorithm operationally simpler to use for forecasters. Research could also be be conducted to determine if Z_{DR} needs to be tuned differently in different locations (this may be an issue of the threshold being met too easily, similar to the Z threshold as discussed earlier). Finally, the data and results from this study could be applied to a lightning cessation study. Similar to lightning initiation, more work must be conducted on applying dual-polarization parameters to the challenging task of forecasting lightning cessation. Studies by Preston and Fuelberg (2012) and Patton (2017) provide more insight into this difficult problem. Although the results of this study highlight the applicability of a current lightning initiation prediction

algorithm, additional research must be conducted to continue the improvement of lightning initiation forecasts.

Bibliography

Ahrens, C. D. (2014). *Meteorology Today: An Introduction to Weather, Climate, and the Environment*. Cengage Learning, 10th edition.

Atlas, D. and Banks, H. C. (1951). The interpretation of microwave reflections from rainfall. *J. Meteor.*, 8:271–282.

Barnes, L. R., Schultz, D. M., Gruntfest, E. C., Hayden, M. H., and Benight, C. C. (2009). CORRIGENDUM: false alarm rate or false alarm ratio? *Wea. Forecasting*.

Bringi, V. N. and Chandrasekar, V. (2001). *Polarimetric Doppler Weather Radar: Principles and Applications*. Cambridge University Press, Cambridge, UK.

Bringi, V. N., Knupp, K., Detwiler, A., Liu, . L., Caylor, I. J., and Black, R. A. (1997). Evolution of a Florida thunderstorm during the convection and precipitation/electrification experiment: the case of 9 August 1991.

Bringi, V. N., Seliga, T. A., and Aydin, K. (1984). Hail detection with a differential reflectivity radar. *Science*, 225:1145–1157.

Buechler, D. E. and Goodman, S. J. (1990). Echo size and asymmetry: impact on NEXRAD storm identification. *J. Appl. Meteor.*, 29:962–969.

Carey, L. D. and Rutledge, S. A. (2000). The relationship between precipitation and lightning in tropical island convection: a c-band polarimetric radar study.

Chmielewski, V. C. and Bruning, E. C. (2016). Lightning Mapping Array flash detection performance with variable receiver thresholds. *J. of Geophys. Res.*, 121(14):8600–8614.

Deierling, W., Latham, J., Petersen, W. A., Ellis, S. M., and Christian Jr., H. J. (2005). On the relationship of thunderstorm ice hydrometeor characteristics and total lightning measurements. *Atmos. Res.*, 76(1-4):114–126.

Deierling, W., Petersen, W. A., Latham, J., Ellis, S., and Christian Jr., H. J. (2008). The relationship between lightning activity and ice fluxes in thunderstorms. *J. Geophys. Res.*, 113(D15).

Dye, J. E., Jones, J. J., and Breed, D. W. (1989). The electrification of New Mexico thunderstorms: 1. relationship between precipitation development and the onset of electrification. *J. Geophys. Res.*, 94:8643–8656.

Efron, B. (1979). Bootstrap methods: another look at the jackknife. *The Annals of Statistics*, 7(1):1–26.

Efron, B. and Tibshirani, R. J. (1993). *An Introduction to the Bootstrap*. Chapman & Hall/CRC, Boca Raton.

Emersic, C. (2006). Investigations into thunderstorm electrification processes. *Ph.D.*

Forbes, G. S. (1993). Lightning studies using LDAR and LLP data. In *NASA Technical Reports Server*.

Gremillion, M. S. and Orville, R. E. (1999). Thunderstorm characteristics of cloud-to-ground lightning at the Kennedy Space Center, Florida: a study of lightning initiation signatures as indicated by the WSR-88D. *Wea. Forecasting*, 14.

GRLevelX (2017). GR2Analyst Radar Software.

Hall, M. P. M., Goddard, J. W. F., and Cherry, S. M. (1984). Identification of Hydrometeors and other targets by dual-polarization radar. *Radar Science*, 19:132–140.

Hesterberg, T. C. (2015). What teachers should know about the bootstrap: resampling in the undergraduate statistics curriculum. *Amer. Statistician*, 64(4):371–386.

Holle, R. L. (2016). A summary of recent national-scale lightning fatality studies. *Wea. Clim. Soc.*, 8:35–42.

Illingworth, A. J., Goddard, J. W. F., and Cherry, S. M. (1987). Polarization radar studies of precipitation development in convective storms. *Q. J. Roy. Meteor. Soc.*, 113:343–354.

Iowa State University (2017). Iowa Environmental Mesonet.

Jayaratne, E. R., Saunders, C. P. R., and Hallett, J. (1983). Laboratory studies of the charging of soft-hail during ice crystal interactions. *Q. J. Roy. Meteor. Soc.*, 109(461):609–630.

Johnson, J. T., MacKeen, P. L., Witt, A., Mitchell, E. D., Stumpf, G. J., Eilts, M. D., and Thomas, K. W. (1998). The storm cell identification and tracking algorithm: an enhanced WSR-88D algorithm. *Wea. Forecasting*, 13:263–276.

Jolliffe, I. T. and Stephenson, D. B. (2003). *Forecast Verification: A Practitioners Guide in Atmospheric Science*. John Wiley and Sons, West Sussex, UK.

Kumjian, M. R. (2013a). Principles and applications of dual-polarization weather radar. part I: description of the polarimetric radar variables. *J. Oper. Meteor.*, 1(19):226–242.

Kumjian, M. R. (2013b). Principles and applications of dual-polarization weather radar. part II: warm-and cold-season applications. *J. Oper. Meteor.*, 1(20):243–264.

Larsen, H. and Stansbury, E. (1974). Association of lightning flashes with precipitation cores extending to height 7 km. *J. Atmos. Terres. Phys.*, 36(9):1547–1553.

MacGorman, D. and Rust, W. (1998). *The Electrical Nature of Storms*. Oxford University Press.

Michimoto, K. (1991). A study of radar echoes and their relation to lightning discharges of thunderclouds in the Hokuriku District. part I: observation and analysis of thunderclouds in summer and winter. *J. Meteor. Soc. of Japan*, 69:327–335.

Mosier, R. M., Schumacher, C., Orville, R. E., and Carey, L. D. (2011). Radar nowcasting of cloud-to-ground lightning over Houston, Texas. *Wea. Forecasting*.

NASA (2005). Lightning Mapping Arrays (LMA).

NASA (2017a). DC Lightning Mapping Array Overview.

NASA (2017b). DC LMA Post-Processed Data Archive.

NASA (2017c). DC LMA Real-Time Browse.

National Geographic (2018). Lightning Facts and Information.

National Lightning Safety Institute (2014). Lightning Costs and Losses from Attributed Sources. Technical report.

NCEI (2017). NCEI NEXRAD Radar Inventory.

NOAA (2017a). Interactive Map Tool.

NOAA (2017b). NOAA NEXRAD Information.

NWS (2011). Dual-Polarization Radar.

NWS (2017a). Natural Hazard Statistics.

NWS (2017b). Radar Operations Center.

NWS (2017c). Understanding Lightning: Initiation of a Stepped Leader.

Orloff, J. and Bloom, J. (2014). Bootstrap Confidence Intervals, Class 24, 18.05 Introduction to Probability and Statistics.

Patton, J. R. (2017). Using radar-derived parameters to develop probabilistic guidance for lightning cessation within isolated convection near Cape Canaveral, Florida. *M.S. Thesis*, pages 1–49.

Preston, A. D. and Fuelberg, H. E. (2012). Improving lightning cessation guidance using polarimetric radar data. *22nd International Lightning Detection Conference*.

Rakov, V. A. (2016). *Fundamentals of Lightning*. Cambridge University Press.

Rakov, V. A. and Rachidi, F. (2009). Overview of recent progress in lightning research and lightning protection.

Rakov, V. A. and Uman, M. A. (2003). *Lightning: Physics and Effects*. Cambridge University Press, Cambridge, UK.

Ramachandran, R. (2017). Washington, DC Lightning Mapping Array.

Reynolds, S. E., Brook, M., and Gourley, M. F. (1957). Thunderstorm charge separation. *J. Meteor.*, 14:426–436.

Rinehart, R. E. (2010). *Radar for Meteorologists*. Rinehart Publishing, Nevada, MO.

Rison, B., Krehbiel, P., and Thomas, R. (2017). The New Mexico Tech 3D Lightning Mapping Array.

Roeder, W. P. (2010). The four dimensional lightning surveillance system.

Roeder, W. P. (2012). A statistical model for the inter-annual and intra-annual fatalities from lightning in the U.S. and comparison to other storm phenomena. *4th International Lightning Meteorology Conference*.

Roeder, W. P. (2017). Personal Correspondence.

Roeder, W. P. (2018). Personal Correspondence.

Roeder, W. P. and Pinder, C. S. (1998). Lightning forecasting techniques for Central Florida in support of America's space program. *16th Conference on Weather Analysis and Forecasting*.

Saunders, C. (2008). Charge separation mechanisms in clouds. *Space Sci. Rev.*, 137:335–353.

Taylor, C. (2017). What Is Bootstrapping in Statistics?

The National Severe Storms Laboratory (2017). Severe Weather 101: Lightning Basics.

Thomas, R. J., Krehbiel, P. R., Rison, W., Hunyady, S. J., Winn, W. P., Hamlin, T., and Harlin, J. (2004). Accuracy of the Lightning Mapping Array. *J. of Geophys. Res.*, 109.

Thurmond, K. R. (2014). Operational cloud-to-ground lightning initiation forecasting utilizing s-band dual-polarization radar. *M.S. Thesis*, pages 1–61.

Travis, A. J. (2015). Utilizing four dimensional lightning and dual-polarization radar to develop lightning initiation forecast guidance. *M.S. Thesis*, pages 1–79.

United States Census Bureau (2010). Census Data Mapper.

University of Wyoming (2017). Atmospheric Soundings.

Vincent, B. R., Carey, L. D., Schneider, D., Keeter, K., and Gonski, R. (2003). Using WSR-88D reflectivity data for the prediction of cloud-to-ground lightning: a North Carolina study. *National Wea. Digest*, 27:35–44.

Wallace, J. M. and Hobbs, P. V. (2006). *Atmospheric Science: An Introductory Survey*. Academic Press, San Diego, CA, second edition.

Weather Edge (2001). Everything Weather: Radars.

Whiton, R. C., Smith, P. L., Bigler, S. G., Wilk, K. E., and Harbuck, A. C. (1998a). History of operational use of weather radar by U.S. weather services. part I: the pre-NEXRAD era. *Wea. Forecasting*.

Whiton, R. C., Smith, P. L., Bigler, S. G., Wilk, K. E., and Harbuck, A. C. (1998b). History of operational use of weather radar by U.S. weather services. part II: development of operational doppler weather radars. *Wea. Forecasting*, 13:244–252.

Wiens, K. C. (2007). Thunderstorm electrical structures observed by Lightning Mapping Arrays. *Amer. Meteor. Soc.*

Wilks, D. S. (2011). *Statistical Methods in the Atmospheric Sciences*. Academic Press, Oxford, UK, 3rd edition.

WilmingtonWx (2017). WilmingtonWx GRLevelX Resources.

Wilson, N. (2005). Lightning Mapping Arrays Oklahoma University.

Wolf, P. (2006). Anticipating the initiation, cessation, and frequency of cloud-to-ground lightning, utilizing WSR-88D reflectivity data. *J. Oper. Meteor.*, 1(20).

Woodard, C. J. (2011). Operational lightning forecasting technique development and testing utilizing c-band dual-polarimetric radar. *M.S. Thesis*, pages 1–129.

Woodard, C. J., Carey, L. D., Petersen, W. A., and Roeder, W. P. (2012). Operational utility of dual-polarization variables in lightning initiation forecasting. *J. Oper. Meteor.*, 13(6):79–102.

Yang, Y. H. and King, P. (2010). Investigating the potential of using radar echo reflectivity to nowcast cloud-to-ground lightning initiation over Southern Ontario. *Wea. Forecasting*.

Yuan, T., Remer, L. A., Pickering, K. E., and Yu, H. (2011). Observational evidence of aerosol enhancement of lightning activity and convective invigoration. *Geophys. Research Letters*, 38(4):n/a–n/a.

REPORT DOCUMENTATION PAGE

Form Approved
OMB No. 0704–0188

1. REPORT DATE *(DD–MM–YYYY)*	2. REPORT TYPE	3. DATES COVERED *(From — To)*
02–26–2018	Master's Thesis	Oct 2016 — Mar 2018

4. TITLE AND SUBTITLE

FORECASTING LIGHTNING INITIATION UTILIZING DUAL-POLARIZATION PARAMETERS OVER WASHINGTON, D.C.

5a. CONTRACT NUMBER

5b. GRANT NUMBER

5c. PROGRAM ELEMENT NUMBER

6. AUTHOR(S)

Olsen, Sarah Allison, 2d Lt, USAF

5d. PROJECT NUMBER

5e. TASK NUMBER

5f. WORK UNIT NUMBER

7. PERFORMING ORGANIZATION NAME(S) AND ADDRESS(ES)

Air Force Institute of Technology
Graduate School of Engineering and Management (AFIT/EN)
2950 Hobson Way
WPAFB OH 45433-7765

8. PERFORMING ORGANIZATION REPORT NUMBER

AFIT-ENP-MS-18-M-092

9. SPONSORING / MONITORING AGENCY NAME(S) AND ADDRESS(ES)

45th Weather Squadron
1201 Edward H. White Ste. C-129
Patrick AFB, FL 32925
COMM 321-853-8410
Email: william.roeder@us.af.mil

10. SPONSOR/MONITOR'S ACRONYM(S)

45WS

11. SPONSOR/MONITOR'S REPORT NUMBER(S)

12. DISTRIBUTION / AVAILABILITY STATEMENT

DISTRIBUTION STATEMENT A:
APPROVED FOR PUBLIC RELEASE; DISTRIBUTION UNLIMITED.

13. SUPPLEMENTARY NOTES

14. ABSTRACT

Prior studies by Woodard (2011), Thurmond (2014), and Travis (2015) show that dual-polarization radar can be utilized to identify the presence of hydrometeors necessary for cloud charging. Travis (2015) discovered two parameters, when used together, produced the best results: $Z \geq 36.5$ dBZ and $Z_{DR} \geq 0.31$ at the -10°C height. This study applied the lightning initiation prediction method developed for Cape Canaveral Air Force Station (CCAFS) and NASA Kennedy Space Center (KSC) in Travis (2015) to a new location. The method was tested on 100 isolated, warm season thunderstorms spanning 5 years in and around the Washington D.C. area. Forecast metrics and lead times were calculated and compared to the results of Travis (2015). The results of this study concluded that the lightning initiation prediction algorithm from Travis (2015) for CCAFS/KSC does not perform well for the Washington, D.C. area. This implies that one lightning initiation prediction method cannot be applied across the entire national NEXRAD network.

15. SUBJECT TERMS

Lightning Initiation, Lightning Mapping Array, Dual-Polarization, Lightning Forecasting

16. SECURITY CLASSIFICATION OF:			17. LIMITATION OF ABSTRACT	18. NUMBER OF PAGES	19a. NAME OF RESPONSIBLE PERSON
a. REPORT	b. ABSTRACT	c. THIS PAGE			Maj Omar Nava, AFIT/ENP
U	U	U	U	84	19b. TELEPHONE NUMBER *(include area code)* (937)-255-3636 x4518; omar.nava@afit.edu

Standard Form 298 (Rev. 8–98)
Prescribed by ANSI Std. Z39.18